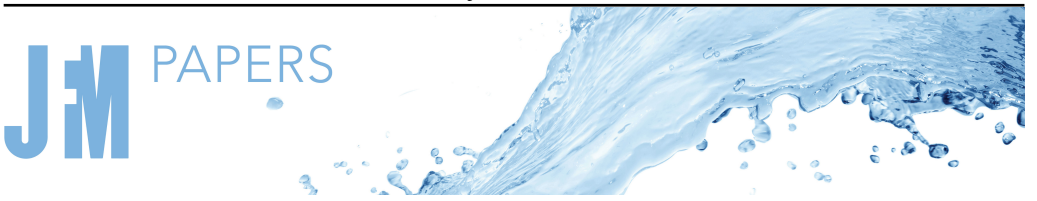
J. Fluid Mech. (2026), *vol.* 1029, A24, doi:10.1017/jfm.2026.11174



Effects of streamwise-grooved spanwise-periodic roughness arrays on boundary-layer instability

Jianing Zheng[1] **and Xuesong Wu**[2,3]

[1]Laboratory of High-Speed Aerodynamics, School of Mechanical Engineering, Tianjin University, Tianjin 300072, PR China

[2]School of Mechanical Engineering, Nantong University, Nantong 226019, PR China

[3]Department of Mathematics, Imperial College London, 180 Queen's Gate, London SW7 2AZ, UK

Corresponding author: Xuesong Wu, x.wu@ic.ac.uk

(Received 23 July 2025; revised 18 December 2025; accepted 19 December 2025)

We investigate the impact of streamwise-grooved and spanwise-periodic surface roughness arrays on the lower-branch viscous Tollmien–Schlichting (TS) instability in the boundary layer over an otherwise flat plate. The streamwise length scale and spanwise spacing of the arrays are of $O(L)$ and $O(Re^{-3/8}L)$, respectively, with the latter being comparable to the characteristic wavelength of the TS modes, where L is the distance from the leading edge of the plate to the peak location of the roughness arrays and Re denotes the Reynolds number based on L, assumed to be large. The characteristic height of the roughness arrays is of $O(Re^{-3/8}L)$, which is greater than the boundary-layer thickness and is the required asymptotic threshold for generating $O(1)$ streaks. We show that this nonlinear streaky flow is governed by three-dimensional (3-D) boundary-layer equations supplemented by a Laplace equation in an inviscid upper deck. Prandtl's transformation is applied to convert the curved boundary to a flat one, which not only reduces computational complexity by avoiding meshing the geometry, but also shows that the spanwise undulation of the roughness arrays enhances transverse diffusion. The Laplace equation is solved to provide the spanwise pressure gradient and velocity, which drive the streaks. The boundary-layer equations are solved efficiently using a streamwise marching scheme. The linear viscous instability of the resulting streaky flow is analysed; by exploiting the asymptotic structure, the bi-global eigenvalue problem is reduced to a one-dimensional one, where the stability is found to be controlled by the spanwise-dependent wall shear and the shape function of the roughness arrays. The results suggest that two-dimensional and weakly 3-D low-frequency modes are stabilised, while most other modes are destabilised. The present formulation provides a convenient tool for predicting streaky flows induced by riblet-like roughness of fairly large height and furthermore assessing their viscous instability properties.

Key words: boundary layer stability, boundary layer control, transition to turbulence

© The Author(s), 2026. Published by Cambridge University Press.

https://doi.org/10.1017/jfm.2026.11174 Published online by Cambridge University Press

1. Introduction

Drag reduction has long been an important goal in aerodynamics for its benefits in reducing fuel consumption and improving vehicle performance. In recent years, spanwise-modulated streamwise-elongated streaks have received much attention due in part to their stabilising effects on Tollmien–Schlichting (TS) instability modes. With weakened instability, transition to turbulence may be delayed and thus drag reduced (Cossu & Brandt 2004; Shahinfar *et al.* 2012; Fransson 2015; Sattarzadeh & Fransson 2017). Among various means of generating streaks, deployment of suitable surface roughness arrays stands out as a promising viable passive control technology as it requires no energy input or electronic components.

The last two decades have seen an increasing amount of literature on streamwise streaks induced by specific forms of roughness arrays. Notably, a number of experimental studies have been carried out. White (2002) and Fransson *et al.* (2004) investigated the evolution of streaks, induced by spanwise-periodic arrays of small circular cross-section and cylindrical roughness elements, respectively. The streamwise and wall-normal distributions of the streaks differ significantly from those of the optimal perturbations, which had been taken as a proxy for physically realisable streaks (Cossu & Brandt 2002, 2004). Fransson *et al.* (2005) found that streaks induced by cylindrical roughness arrays have a stabilising effect on TS modes, with the effect becoming more significant as the streak amplitude is increased (but below a threshold for directly triggering transition). Fransson *et al.* (2006) further showed that by inhibiting the growth of TS modes, such arrays delayed transition to turbulence. Downs & Fransson (2014) investigated streamwise-elongated, spanwise-periodic arrays of roughness elements with hemispherical-cap cross-section, finding that the streamwise extent of the laminar flow was increased by up to 70 % compared with the smooth-wall case.

In order to generate larger-amplitude streaks without triggering bypass transition, Fransson & Talamelli (2012) designed a type of spanwise roughness array called miniature vortex generators (MVGs). Compared with circular roughness elements, MVGs guided the flow in such a way that the absolute instability region behind the device is reduced. The amplitude of the excited streaks exceeded 30 % of the free-stream velocity, a substantial improvement compared with the 12 % reported by Fransson *et al.* (2004). Shahinfar *et al.* (2012) verified that MVGs can generate streaks with nearly twice the amplitude produced by circular roughness elements, and these higher-amplitude streaks are more effective in inhibiting the growth of TS modes. Shahinfar *et al.* (2013) further examined the effects of 15 different MVGs on TS modes propagating through these arrays, finding that MVGs with well-chosen geometrical parameters could effectively suppress the growth of TS modes. Shahinfar, Sattarzadeh & Fransson (2014) demonstrated that finite-amplitude streaks induced by MVGs not only quench two-dimensional (2-D) TS modes but also suppress single and paired oblique modes, successfully delaying transition.

By leveraging numerical methods, researchers have validated the benefits of roughness arrays, especially MVGs, in suppressing flow instabilities, and gained insights into the mechanisms of transition control. Piot, Casalis & Rist (2008) used direct numerical simulation (DNS) to calculate the streaky flow downstream of spanwise-periodic roughness arrays. A subsequent bi-global stability analysis showed that the streaks stabilise TS modes. Similarly, Siconolfi, Camarri & Fransson (2015) conducted bi-global stability analysis of MVG-induced streaky flow calculated also by DNS. They found that the geometric discontinuity of the MVGs causes an unstable region near their trailing edge. However, downstream of this region, the growth of TS modes is suppressed. Szabó *et al.*

https://doi.org/10.1017/jfm.2026.11174 Published online by Cambridge University Press

(2024) used DNS to calculate the flow in the vicinity of MVGs. So-called boundary-region equations were employed to describe the downstream evolution of the streaky boundary layer, and a bi-global stability analysis was then performed. Numerical results show that optimising MVG parameters can avoid initial higher streak amplitudes that may cause secondary instabilities, allowing the streaks to extend farther downstream and attenuate TS modes more efficiently.

Experimental and numerical findings have inspired theoretical studies aimed at understanding mechanisms of transition delay. Using a high-Reynolds-number asymptotic approach, Kátai & Wu (2020) investigated effects of streamwise-elongated and spanwise-periodic roughness arrays on the lower-branch TS instability in the incompressible regime. The roughness-induced streaky flow was found to be governed by a streamwise-parabolic system, which is much simpler than the elliptic system for roughness elements with the streamwise and spanwise length scales both being of $O(Re^{-3/8}L)$ (Smith, Sykes & Brighton 1977). By exploiting the asymptotic structure in the wall-normal direction, the bi-global stability was reduced to a one-dimensional eigenvalue problem, which showed that the instability is controlled directly by the spanwise-dependent wall shear. The 2-D and weakly three-dimensional (3-D) low-frequency TS modes are stabilised while strongly 3-D modes and higher-frequency modes are destabilised. Similar conclusions were drawn by Zhu & Wu (2022) and Zheng & Wu (2024), who used the same asymptotic framework to investigate the impact of streamwise-elongated heating and roughness elements on supersonic boundary-layer instability, respectively. In both cases, the streaky supersonic boundary layers were found to support radiating modes, which emit spontaneous sound waves to the far field; this observation was also made by Liu *et al.* (2022) and Bi *et al.* (2023).

The high-Reynolds-number asymptotic approach is complementary to finite-Reynolds-number calculations of DNS and full bi-global calculations (Piot *et al.* 2008; Siconolfi *et al.* 2015; Bi *et al.* 2023; Szabó *et al.* 2024). The latter are costly and technically challenging. In contrast, the asymptotic approach establishes simplified mathematical systems in which the induced streaky flow and its lower-branch viscous instability can be studied expeditiously and at a much reduced cost, and furthermore, *a priori* insight can be obtained, as has been demonstrated in previous studies (Kátai & Wu 2020; Zhu & Wu 2022; Zheng & Wu 2024). These advantages are of course gained at the expense of quantitative accuracy.

Based on these observations, we adopt the asymptotic framework to study the lower-branch viscous instability of the streaky boundary layer induced by streamwise-grooved and spanwise-periodic roughness arrays with an $O(Re^{-3/8}L)$ spanwise scale but a streamwise scale of $O(L)$, which is much longer than those considered by Kátai & Wu (2020) and Zheng & Wu (2024). Such roughness arrays are riblet-like in the sense that the streamwise length is much longer than the spanwise spacing, and they are of both theoretical and practical interest. The induced streaky flow exhibits an asymptotic structure different from that in previous studies. In practice, highly elongated roughness arrays are common. We note in particular that in the experiments of Downs & Fransson (2014), the roughness arrays extend in the streamwise direction over a significant fraction of L, and as a result the scaling in Kátai & Wu (2020) and Zheng & Wu (2024) is not the most appropriate.

The rest of the paper is organised as follows. In § 2, we formulate the problem and derive the nonlinear system governing the roughness-induced streaky flow. In § 3, the numerical methods for solving the system are described. The numerical set-up is described in § 4 for three forms of roughness arrays: streamwise-Gaussian and spanwise-sinusoidal;

https://doi.org/10.1017/jfm.2026.11174 Published online by Cambridge University Press

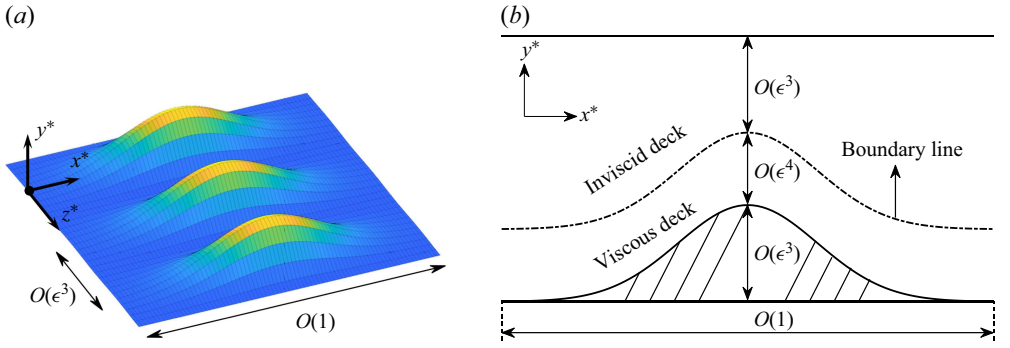


Figure 1. Schematic diagram of (*a*) riblet-like roughness arrays and (*b*) asymptotic structure of the roughness-induced streaky flow.

streamwise step-like and spanwise hemispheric; and streamwise step-like and spanwise-sinusoidal. The first is an idealised configuration having a simpler parametrisation and is thus suitable for demonstrating generic features of the streaks and their stability, while the second is considered for comparison with the experiments of Downs & Fransson (2014). Numerical results for the streaky boundary layer are presented in § 5. In § 6, we conduct a linear stability analysis of the streaky flow, reducing the bi-global eigenvalue problem to a one-dimensional one, which shows that the instability is controlled by the spanwise-dependent wall shear and the shape function of the roughness elements. Stability results are presented in § 7, and conclusions are given in § 8.

2. Formulation

We investigate an incompressible boundary-layer flow over a flat plate where arrays of streamwise-grooved, spanwise-periodic surface roughness are deployed. The height of the roughness is assumed to increase monotonically from a vanishing small value at the leading edge, reaching its peak at a distance L downstream (see figure 1*a*). The streaky flow and ensuing instability are described using the dimensionless Cartesian coordinates (x^*, y^*, z^*) with the origin at the leading edge of the plate, where x^*, y^* and z^* measure the streamwise, wall-normal and spanwise distances, respectively, all non-dimensionalised by L. The velocities and pressure, denoted by (u^*, v^*, w^*) and p^*, are non-dimensionalised by the free-stream velocity U_∞ and the dynamic pressure ρU_∞^2, where ρ is the fluid density. The geometry of the roughness array is specified as $y^* = h^* F(x^*, z^*)$, where h^* represents the height and F describes the shape of the roughness elements. We define the Reynolds number Re as $Re = \rho U_\infty L/\mu$, where μ is the viscosity coefficient. Taking $Re \gg 1$, we define the small parameter $\epsilon = Re^{-1/8}$.

Our focus is on roughness arrays with streamwise and spanwise length scales of $O(1)$ and $O(\epsilon^3)$, respectively, as shown in figure 1(*a*), with the length scales being normalised by L. The spanwise spacing of the roughness arrays is chosen to be comparable to the spanwise length scale of the lower-branch viscous instability that exists in the flat-plate case. Roughness arrays on this scale are distinguished as they could exert a direct impact on the instability; roughness arrays with a different spanwise spacing would be less effective. The asymptotic structure for the induced 3-D flow can be deduced from the well-known triple-deck structure, via a rescaling procedure pertinent to the increased streamwise scale from $O(\epsilon^3)$ to $O(1)$. To generate a fully nonlinear 3-D flow, the asymptotic threshold height of the roughness arrays must be of $O(\epsilon^3)$. The flow acquires an asymptotic structure consisting of two layers, the viscous and inviscid layers (decks), as is shown in figure 1(*b*).

https://doi.org/10.1017/jfm.2026.11174 Published online by Cambridge University Press

Our chosen scale is a limiting case in Kátai & Wu (2020), where the rescaling procedure leading to the asymptotic structure was given. The rescaling was carried out by introducing a streamwise stretch factor, ϵ_1, the ratio of the spanwise spacing to the streamwise scale of the roughness arrays, and taking ϵ_1 to be asymptotically small. The present study corresponds to the distinguished case of $\epsilon_1 = O(\epsilon^3)$, for which the threshold roughness height for generating nonlinear streaks is $h^* = O(\epsilon^3)$ according to the scaling $h^* = O(\epsilon^5 \epsilon_1^{-2/3})$ in Kátai & Wu (2020), and the lower deck merges with the main deck, resulting in a two-layered structure rather than the triple deck. The asymptotic structure and governing equations can alternatively be deduced directly by considering the Navier–Stokes (NS) equations.

2.1. *Nonlinear formulation for the roughness-induced steady flow*

We formulate the equations for these two decks, starting with the viscous deck, which is a thin layer with $O(\epsilon^4)$ width above a curved wall $y^* = h^* F$. The derivation of the governing equations is facilitated by introducing appropriately rescaled coordinates:

$$x = x^* = O(1), \quad Y = \epsilon^{-4}(y^* - h^* F) = O(1), \quad Z = \epsilon^{-3} z^* = O(1), \tag{2.1a–c}$$

where Prandtl's transformation (Prandtl 1938) has been implemented to convert the curved boundary to $Y = 0$. The velocities and pressure are scaled as

$$(u^*, v^* - h^* u^* F_{x^*} - h^* w^* F_{z^*}, w^*, p^*) = (U, \epsilon^4 V, \epsilon^3 W, \epsilon^6 P)(x, Y, Z) + \text{h.o.t.}, \tag{2.2}$$

where h.o.t. stands for high-order terms in the expansion that have not been written out explicitly; such a convention is followed throughout the paper. Substitution of (2.1) and (2.2) into the NS equations leads to the leading-order governing equations:

$$\frac{\partial U}{\partial x} + \frac{\partial V}{\partial Y} + \frac{\partial W}{\partial Z} = 0, \tag{2.3a}$$

$$U\frac{\partial U}{\partial x} + V\frac{\partial U}{\partial Y} + W\frac{\partial U}{\partial Z} = \left(1 + h^2 F_Z^2\right)\frac{\partial^2 U}{\partial Y^2}, \tag{2.3b}$$

$$U\frac{\partial W}{\partial x} + V\frac{\partial W}{\partial Y} + W\frac{\partial W}{\partial Z} = -\frac{\partial P}{\partial Z} + \left(1 + h^2 F_Z^2\right)\frac{\partial^2 W}{\partial Y^2}, \tag{2.3c}$$

plus $\partial P/\partial Y = 0$, indicating that $P = P(x, Z)$. Here, the subscript Z represents the spanwise derivative, and $h = O(1)$ is the rescaled height, introduced via

$$h^* = \epsilon^3 h. \tag{2.4}$$

It is worth adding that in the wall-normal momentum equation, the pressure gradient $\partial p/\partial y^* = O(\epsilon^2)$ in view of (2.1*b*) and (2.2), while the inertia is dominated by the centrifugal force due to the streamwise and spanwise curvatures of the roughness arrays, represented by $-u^{*2} h^* F_{x^* x^*} - w^{*2} h^* F_{z^* z^*}$, which is of $O(\epsilon^3)$ according to (2.1)–(2.2) and (2.4). It follows that $\partial P/\partial Y = 0$ to leading-order accuracy. The no-slip boundary condition and the far-field matching condition are imposed as

$$U = V = W = 0 \quad \text{at} \quad Y = 0; \tag{2.5a}$$

$$U \to 1, \quad W \to W_\infty \quad \text{as} \quad Y \to \infty. \tag{2.5b,c}$$

The system (2.3) with (2.5) can be solved when the pressure gradient $\partial P/\partial Z$ in (2.3*c*) and the velocity W_∞ in (2.5*c*) are determined by matching with the inviscid-deck solution.

It is worth noting that in (2.3*b*,*c*), the coefficients of the viscous terms are modified to $1 + h^2 F_Z^2$, with the extra terms proportional to $h^2 F_Z^2$ arising from applying Prandtl's transformation and being contributed by the spanwise diffusion terms in the momentum

https://doi.org/10.1017/jfm.2026.11174 Published online by Cambridge University Press

equations. This is a geometric effect and may be interpreted as the spanwise modulation of roughness arrays causing enhanced equivalent transverse diffusion relative to the flat-plate case. This is an interesting effect that does not appear to have been noted previously. Although a similar enhanced (modified) transverse diffusion arises due to the streamwise modulation of a 2-D surface roughness (Hanevy *et al.* 2024). In the cited work, for the modification to be a leading-order effect, the roughness height must be very large, of $O(1)$, whereas in the present problem, the roughness height and spanwise spacing are both of $O(\epsilon^3)$ (so that the spanwise slope is of $O(1)$). Since the extra terms in (2.3*b*,*c*) originate from the spanwise diffusion, the system (2.3) has gone beyond the classical boundary-layer equations. In the streamwise momentum equation (2.3*b*), the pressure gradient is absent because it is of $O(\epsilon^6)$, significantly smaller than the $O(1)$ inertial and viscous terms. Consequently, the system (2.3) is streamwise parabolic, and so can be solved numerically using an efficient streamwise marching method. In addition, meshing a domain over a curved boundary is avoided after applying Prandtl's transformation. Due to these two features, the streaky flow can be obtained at a significantly reduced computation cost than performing DNS.

Prandtl's transformation in (2.2) indicates that the displacement due to the roughness drives a wall-normal velocity at the outer edge of the boundary layer:

$$v^*_\infty = \epsilon^3 h(F_x + W_\infty F_Z) \quad \text{as} \quad Y \to \infty. \tag{2.6}$$

This so-called transpiration velocity forces $O(\epsilon^3)$ perturbations outside the boundary layer. The 3-D components reside primarily in the inviscid deck with $O(\epsilon^3)$ width and attenuate there. However, if the roughness shape contains a 2-D (spanwise-averaged) component, denoted as $F_{x,2D}$, the induced 2-D disturbance, also of $O(\epsilon^3)$, attenuates more slowly in the extended outer region occupying a vertical thickness of $O(1)$. We expand and scale the velocities and pressure as

$$(u^*, v^*, w^*, p^*) = \left(1 + \epsilon^3 \bar{u}(x, y^*), \epsilon^3 \bar{v}(x, y^*), 0, P_B + \epsilon^3 \bar{p}(x, y^*)\right) + \text{h.o.t.} \tag{2.7}$$

Substitution of (2.7) into the NS equations leads to the leading-order equations:

$$\frac{\partial \bar{u}}{\partial x} + \frac{\partial \bar{v}}{\partial y^*} = 0, \quad \frac{\partial \bar{u}}{\partial x} = -\frac{\partial \bar{p}}{\partial x}, \quad \frac{\partial \bar{v}}{\partial x} = -\frac{\partial \bar{p}}{\partial y^*}. \tag{2.8a–c}$$

The matching condition between the outer region and the boundary layer, and the far-field condition are

$$\bar{v} \to h F_{x,2D} \quad \text{as} \quad y^* \to 0; \quad (\bar{u}, \bar{v}, \bar{p}) \to 0 \quad \text{as} \quad y^* \to \infty. \tag{2.9a,b}$$

The inviscid deck outside the boundary layer occupies the region with a width of $O(\epsilon^3)$, which is determined by the spanwise spacing of the roughness arrays. The wall-normal velocity in this layer is also of $O(\epsilon^3)$, determined by the transpiration velocity (2.6). Moreover, an order-of-magnitude analysis of the continuity and spanwise momentum equations reveals that the spanwise velocity and pressure are of $O(\epsilon^3)$ and $O(\epsilon^6)$, respectively. Thus, we introduce the rescaled wall-normal coordinate $y = \epsilon^{-3} y^*$, and scale the velocities and pressure as

$$(u^*, v^*, w^*, p^*) = (1 + \epsilon^3 u, \epsilon^3 v, \epsilon^3 w, \epsilon^6 p)(x, y, Z) + \text{h.o.t.} \tag{2.10}$$

https://doi.org/10.1017/jfm.2026.11174 Published online by Cambridge University Press

Substituting (2.10) into the NS equations written in terms of (x, y, Z) results in the simplified equations

$$\frac{\partial v}{\partial y} + \frac{\partial w}{\partial Z} = 0, \tag{2.11a}$$

$$\frac{\partial v}{\partial x} + v\frac{\partial v}{\partial y} + w\frac{\partial v}{\partial Z} = -\frac{\partial p}{\partial y}, \tag{2.11b}$$

$$\frac{\partial w}{\partial x} + v\frac{\partial w}{\partial y} + w\frac{\partial w}{\partial Z} = -\frac{\partial p}{\partial Z}, \tag{2.11c}$$

where the streamwise momentum equation is not needed. These equations are strongly nonlinear unlike their counterparts in most multi-layered (triple- or double-deck) structures. As the transverse extent of the present inviscid layer is comparable to the roughness height, the 'boundary surface' between the viscous and inviscid decks is located at $y = hF$. The matching conditions between the two are

$$v = h(F_x + W_\infty F_Z), \quad w = W_\infty \quad \text{at} \quad y = hF. \tag{2.12a,b}$$

The far-field condition reads

$$v \to hF_{x,2D}, \quad w \to 0 \quad \text{as} \quad y \to \infty, \tag{2.13}$$

where the first indicates the matching with the roughness-induced 2-D component attenuating slowly in the outer region.

Equations (2.3) and (2.11) along with conditions (2.5) and (2.12)–(2.13) form a closed nonlinear system describing the roughness-induced streaky flow. As scaling (2.4) indicates, the system is applicable in principle to roughness arrays with heights greater than the boundary-layer thickness, and to the best of our knowledge has not been derived before. The formulation shows that the elongated roughness arrays distort streamlines thereby generating a transpiration velocity v at the outer edge of the boundary layer; see (2.12*a*). The blowing induces the spanwise pressure gradient p_Z and velocity w in the inviscid deck, which in turn act on the viscous layer; see (2.3*c*) and (2.5*c*).

The streaky flow supports viscous instability, whose characteristic streamwise and spanwise wavelengths are of $O(\epsilon^3)$. This stability problem is formulated in § 6. Next we consider the numerical methods for solving the nonlinear system governing the streaky flow.

3. Numerical procedures

Based on the distinct properties of each set of equations in the nonlinear system, we adopt specialised numerical methods to achieve both computational efficiency and accuracy.

3.1. *Inviscid deck*

The continuity (2.11*a*) allows for introduction of a streamfunction ψ, defined as

$$v = \psi_Z, \quad w = -\psi_y. \tag{3.1a,b}$$

Subtracting the derivative of (2.11*c*) with respect to y from the derivative of (2.11*b*) with respect to Z, followed by substituting (3.1) into the resulting equation, we obtain

$$\frac{\partial \nabla^2\psi}{\partial x} - \frac{\partial \psi}{\partial y}\frac{\partial \nabla^2\psi}{\partial Z} + \frac{\partial \psi}{\partial Z}\frac{\partial \nabla^2\psi}{\partial y} = 0. \tag{3.2}$$

Equation (3.2) indicates that the material derivative $\mathrm{d}\Omega/\mathrm{d}x = 0$, where the vorticity $\Omega = \nabla^2\psi$. As $x \to 0$, $\Omega \to 0$. It follows that $\Omega = 0$ for all $x > 0$ in the region above

https://doi.org/10.1017/jfm.2026.11174 Published online by Cambridge University Press

the surface $y = hF$, i.e. the inviscid flow field is irrotational and so ψ satisfies the Laplace equation

$$\nabla^2\psi = 0. \tag{3.3}$$

In view of the matching condition (2.12*a*) or the far-field condition (2.13), which is contingent on the existence of a 2-D component in the roughness arrays, (3.3) admits the solution

$$\psi(y, Z) = a_0 Z + \sum_{k=-\infty, k\neq 0}^{\infty} a_k \mathrm{e}^{-|k|\beta y}\mathrm{e}^{\mathrm{i}k\beta Z}, \tag{3.4}$$

where the first term represents the 2-D component and $|k|$ ensures attenuation of 3-D components in the far field. The non-periodic term $a_0 Z$ amounts to a wall-normal velocity a_0, which is a constant in the present inviscid deck, consistent with the fact that this 2-D velocity attenuates slowly over much longer vertical distances. Note that the streamfunction ψ is non-periodic, but the physical quantities, the velocity and pressure, are periodic. The solution (3.4) can be recast in terms of the transformed wall-normal coordinate $\bar{y} = y - hF$:

$$\begin{aligned}\psi(\bar{y}, Z) &= a_0 Z + \sum_{k=-\infty, k\neq 0}^{\infty} a_k \mathrm{e}^{\mathrm{i}k\beta Z - |k|\beta hF}\mathrm{e}^{-|k|\beta\bar{y}} \\ &= a_0 Z + \sum_{n=-\infty}^{\infty}\sum_{k=-\infty, k\neq 0}^{\infty} a_k d_{kn}\mathrm{e}^{-|k|\beta\bar{y}}\mathrm{e}^{\mathrm{i}n\beta Z},\end{aligned} \tag{3.5}$$

where d_{kn} are obtained by expanding $\mathrm{e}^{\mathrm{i}k\beta Z - |k|\beta hF}$ into the Fourier series

$$\mathrm{e}^{\mathrm{i}k\beta Z - |k|\beta hF} = \sum_{n=-\infty}^{\infty} d_{kn}\mathrm{e}^{\mathrm{i}n\beta Z}. \tag{3.6}$$

In terms of the shifted coordinate $(\bar{y}, Z)$, the boundary condition (2.12) becomes

$$\frac{\partial\psi}{\partial Z} = hF_x \quad \text{at} \quad \bar{y} = 0, \tag{3.7}$$

which is directly determined by h and F, independent of the hitherto unknown W_∞. This leads to decoupling of the numerical procedures for the inviscid and viscous decks. Substituting (3.5) into (3.7) and expanding $F_x(x, Z)$ into a Fourier series, $F_x(x, Z) = \sum f_{x,n}\mathrm{e}^{\mathrm{i}n\beta Z}$, we find that $a_0 = hf_{x,0} = hF_{x,2D}$, and for $n \neq 0$

$$\mathrm{i}n\beta \sum_{k=-\infty, k\neq 0}^{\infty} a_k d_{kn} = hf_{x,n}. \tag{3.8}$$

The coefficients a_k $(k \neq 0)$ are obtained by solving the truncated system (3.8) with $-K \leqslant k \leqslant K$, where $K \geqslant 16$ is found to ensure adequate accuracy of the solution. The streamfunction ψ is then reconstructed using (3.5). The velocities v and w can be computed from (3.1), and in particular $W_\infty = w|_{y=hF}$ is found. The pressure gradients, $\partial p/\partial y$ and $\partial p/\partial Z$, are determined using (2.11*b*,*c*). As mentioned earlier, the values of w and $\partial p/\partial Z$ at the 'boundary surface' are used to solve the viscous-deck equations (2.3). It is worth noting that the inviscid flow is controlled by f_x, the streamwise slope of the roughness, as (3.8) indicates. It is thus expected that there would be a reversal of the signs of w and $\partial p/\partial Z$ past the peak of the roughness.

https://doi.org/10.1017/jfm.2026.11174 Published online by Cambridge University Press

3.2. *Viscous streaky boundary layer*

The system of boundary-layer equations, (2.3), does not admit a self-similar solution due to the spanwise modulation caused by roughness arrays. Nevertheless, it is convenient to rearrange the equations in (2.3) using the similarity variable and the streamfunctions:

$$\eta = x^{-1/2}Y, \quad \frac{\partial f}{\partial \eta} = U, \quad \frac{\partial g}{\partial \eta} = W. \tag{3.9a–c}$$

Substitution of (3.9) into (2.3*a*) followed by integration with respect to η yields

$$x\frac{\partial f}{\partial x} - \frac{1}{2}\eta U + \frac{1}{2}f + x^{1/2}V + x\frac{\partial g}{\partial Z} = 0, \tag{3.10}$$

where use has been made of the no-slip condition and the fact that $f = g = 0$ at $\eta = 0$. Substituting (3.9) into (2.3*b*,*c*) and using (3.10) to eliminate V, we have

$$xU\frac{\partial U}{\partial x} - \left(x\frac{\partial f}{\partial x} + x\frac{\partial g}{\partial Z} + \frac{1}{2}f\right)\frac{\partial U}{\partial \eta} + xW\frac{\partial U}{\partial Z} = \left(1 + h^2F_Z^2\right)\frac{\partial^2 U}{\partial \eta^2}, \tag{3.11a}$$

$$xU\frac{\partial W}{\partial x} - \left(x\frac{\partial f}{\partial x} + x\frac{\partial g}{\partial Z} + \frac{1}{2}f\right)\frac{\partial W}{\partial \eta} + xW\frac{\partial W}{\partial Z} = -xP_Z + \left(1 + h^2F_Z^2\right)\frac{\partial^2 W}{\partial \eta^2}. \tag{3.11b}$$

Furthermore, the roughness-induced streaky flow is decomposed as

$$(f, g, U, W) = (f_B, 0, U_B, 0) + (f_1, g_1, U_1, W_1), \tag{3.12}$$

where the first part represents the Blasius solution, which satisfies the equations

$$-\frac{1}{2}f_B\frac{\partial U_B}{\partial \eta} = \frac{\partial^2 U_B}{\partial \eta^2}, \quad \frac{\partial f_B}{\partial \eta} = U_B, \tag{3.13a,b}$$

with the boundary conditions $f_B(0) = U_B(0) = 0$ and $U_B(\infty) = 1$. The second part in (3.12) denotes the roughness-induced flow with $U_1 = \partial f_1/\partial \eta$ and $W_1 = \partial g_1/\partial \eta$. Substitution of (3.12) and (3.13) into (3.11) leads to the coupled equations

$$xU_B\frac{\partial U_1}{\partial x} - \frac{1}{2}f_B\frac{\partial U_1}{\partial \eta} - \frac{\partial^2 U_1}{\partial \eta^2} = N(U_1) + L(U_B), \tag{3.14a}$$

$$xU_B\frac{\partial W_1}{\partial x} - \frac{1}{2}f_B\frac{\partial W_1}{\partial \eta} - \frac{\partial^2 W_1}{\partial \eta^2} = -xP_Z + N(W_1), \tag{3.14b}$$

where

$$N(\bullet) = L(\bullet) - xU_1\frac{\partial \bullet}{\partial x} - xW_1\frac{\partial \bullet}{\partial Z}, \tag{3.15a}$$

$$L(\bullet) = h^2F_Z^2\frac{\partial^2 \bullet}{\partial \eta^2} + \left(\frac{1}{2}f_1 + x\frac{\partial f_1}{\partial x} + x\frac{\partial g_1}{\partial Z}\right)\frac{\partial \bullet}{\partial \eta}. \tag{3.15b}$$

The boundary and matching conditions in terms of η are specified as

$$U_1 = W_1 = 0 \quad \text{at} \quad \eta = 0; \quad (U_1, W_1) \to (0, w|_{\tilde{y}=0}) \quad \text{as} \quad \eta \to \infty. \tag{3.16a,b}$$

After rearranging and decomposing, the resulting equations (3.14) have better numerical stability and are convenient for implementing a streamwise marching scheme.

The parabolic system (3.14) is to be solved with an appropriate upstream condition. For this purpose, we consider roughness arrays whose rescaled height $F(x, Z) \to 0$ as $x \to 0$. For simplicity, the wall shape is taken to be of the variable-separation form:

$$F(x, Z) = F_f(x)F_g(Z). \tag{3.17}$$

https://doi.org/10.1017/jfm.2026.11174 Published online by Cambridge University Press

Roughness arrays of the above form with suitable F_f and F_g may represent those in experiments (e.g. Downs & Fransson 2014). The initial conditions for two forms of F_f and their constructions are provided in Appendix A. It is worth pointing out the mathematical formulation is valid, and numerical solutions can be obtained, for a general roughness shape $F(x, Z)$, which always assumes the form (3.17) in the upstream limit, as can be shown by Taylor expansion of $F(x, Z)$ for $x \ll 1$.

Given that the roughness arrays are spanwise-periodic, so is the induced streaky flow. Its solution (f_1, g_1, U_1, W_1) is thus expanded into Fourier series:

$$(f_1, g_1, U_1, W_1) = \sum_{n=-\infty}^{\infty} (\hat{f}_n, \hat{g}_n, \hat{U}_n, \hat{W}_n) \exp(\mathrm{i}n\beta Z), \tag{3.18}$$

where β represents the spanwise wavenumber of the roughness arrays so that the spanwise wavelength $\Lambda = 2\pi/\beta$. Substituting (3.18) into (3.14) results in

$$xU_B \frac{\partial \hat{U}_n}{\partial x} - \frac{1}{2} f_B \frac{\partial \hat{U}_n}{\partial \eta} - \frac{\partial^2 \hat{U}_n}{\partial \eta^2} = [\mathcal{F}(N(U_1) + L(U_B))]_n \,, \tag{3.19a}$$

$$xU_B \frac{\partial \hat{W}_n}{\partial x} - \frac{1}{2} f_B \frac{\partial \hat{W}_n}{\partial \eta} - \frac{\partial^2 \hat{W}_n}{\partial \eta^2} = [\mathcal{F}(-xP_Z + N(W_1))]_n \,, \tag{3.19b}$$

$$\hat{U}_n = \frac{\partial \hat{f}_n}{\partial \eta}, \quad \hat{W}_n = \frac{\partial \hat{g}_n}{\partial \eta}, \tag{3.19c,d}$$

where $\mathcal{F}$ denotes a discrete-Fourier-transformed quantity. Equations (3.19) are truncated by retaining $2K$ terms in the Fourier series, and discretised in the streamwise and wall-normal directions using the Crank–Nicolson scheme.

The solution procedure for solving (3.19) is as follows. First, the right-hand terms (except the pressure gradient) in (3.19*a*,*b*) at the second streamwise position are estimated using the velocity field at the initial streamwise position, given by the similarity solution (A9). Equations (3.19*b*) and (3.19*a*) are solved sequentially to obtain W_1 and U_1 on each $\eta - Z$ slice. Then, (3.19*c*,*d*) are used to solve for f_1 and g_1. After the velocities and streamfunctions are predicted, the right-hand terms except the pressure gradient are evaluated again in physical space and subsequently transformed back to spectral space, where an enhanced version of the so-called 2/3 rule (Orszag 1971) is used to eliminate aliasing errors. Next, due to nonlinearity, the velocities are updated iteratively until the difference between consecutive estimates falls below a predefined tolerance of 10^{-8}. This iterative process yields the solution at each streamwise position. The computational domain is $[0.01, 2] \times [0, 40]$ with step sizes of $\Delta x = 0.001$ and $\Delta\eta = 0.05$. In the spanwise direction, use of $2K = 64$ Fourier modes proves to suffice for capturing the nonlinear effect at most locations. However, close to the boundary-layer separation, the number of Fourier modes needs to be increased to $2K = 256$. Calculations on different grids are performed to ensure that the numerical results are mesh-independent. The running time for each case is approximately six hours (on an Intel i7-10700 8-core processor).

4. Numerical set-up

We perform calculations for three forms of roughness arrays. The first of these configurations is characterised by a Gaussian-like profile in the streamwise direction and

https://doi.org/10.1017/jfm.2026.11174 Published online by Cambridge University Press

Normalised parameters	Downs & Fransson (2014)	Present study
$h=\epsilon^{-3}h^+/L$	0.279	0.055−0.22
$\Lambda=\epsilon^{-3}\Lambda^+/L$	≈2.1/4.2/8.4	2.2/4.4/8.8
$L_x=l_x^+/L$	≈0.59	≈0.6
$\epsilon=Re^{-1/8}$	≈0.2036	0.2036
$F_r=10^6\epsilon^6\omega$	100	35−210
ω	≈1.4	0.5−3

Table 1. The non-dimensional parameters pertinent to the experiment of Downs & Fransson (2014) and those used in our calculations: the distance to the leading edge, $L=425$ mm; dimensional roughness height, $h^+=1$ mm; spanwise spacing, $\Lambda^+=7.5$, 15 and 30 mm; roughness length, $l_x^+=250$ mm; Reynolds number, $Re=3.4\times10^5$; dimensionless frequency, $F_r=2\pi\nu f^+\times10^6/U_\infty^2$, where f^+ and ω denote the dimensional and normalised frequencies of the instability wave, respectively.

is sinusoidal in the spanwise direction. The shape function is defined by (3.17) with

$$F_f(x)=x^2\exp(-(x-1+d^2)^2/d^2+d^2),\quad F_g(Z)=\frac{1}{2}\cos(\beta Z),\tag{4.1}$$

where d controls the shape of the Gaussian. The parameters are determined based on the experimental configuration with a streamwise length of 250 mm, as listed in table 1. The parameter d is set to 0.2, yielding an effective streamwise length of 0.6, defined as the interval between the two positions where the roughness height is one-tenth of its maximum. The value is close to the experimental parameter $L_x=l_x^+/L\approx0.59$.

The second form of roughness arrays features a streamwise step-like geometry and a spanwise hemispherical cap, which closely replicates the experimental configuration in Downs & Fransson (2014). The roughness profile is represented by

$$F_f(x)=\frac{1}{2}\left[\tanh\left(\frac{x-1+l_x}{d_x}\right)-\tanh\left(\frac{x-1-l_x}{d_x}\right)\right],\tag{4.2}$$

$$F_g(Z)=\begin{cases}\left(\sqrt{d_z^2-Z^2}-d_z+h_z\right)/h_z & \text{for}\quad -l_z<Z<l_z,\\ 0 & \text{otherwise,}\end{cases}\tag{4.3}$$

where d_x and l_x characterise the steepness of the slopes and the streamwise length of the roughness element, respectively. The parameters d_z, h_z and $l_z=\sqrt{d_z^2-(d_z-h_z)^2}$ denote the radius of the circle, the height and half-spanwise width of the hemispherical cap, respectively. The experiments were conducted for the two streamwise lengths, $l_x^+=250$ and 480 mm, both having a radius of $d_z^+=5$ mm, height $h_z^+=1$ mm and width $2l_z^+=6$ mm. These parameters are converted to the non-dimensional parameters in the theory via the relations $(d_z,h_z,l_z)=\epsilon^{-3}(d_z^+,h_z^+,l_z^+)/L$ and $l_x=l_x^+/(2L)$. The resulting normalised parameters (d_z,h_z,l_z) and l_x together with d_x, which is chosen to approximate the rounding of the leading and trailing edges of the step, are summarised in table 2, and they are used in our computations. Note that a strict step would introduce short local streamwise length scales of $O(\epsilon^3)$ or smaller near the sharp edges (Smith & Walton 1998), violating the assumed scale disparity. This scenario was avoided in our work as the forward and backward steps are smoothed out over a length d_x, which is sufficiently small to capture the essential 'step-like' feature, but not too small ($d_x\gg\epsilon^3$) so that potential inviscid–viscous interaction is avoided and the evolution of the streaks remains being governed by the parabolic system of the boundary-layer equations. The theoretical results

https://doi.org/10.1017/jfm.2026.11174 Published online by Cambridge University Press

Parameters	l_x	d_x	d_z	h_z	l_z
Roughness 2 (250 mm)	0.28	0.1	1.4	0.28	0.84
Roughness 2 (480 mm)	0.4	0.1	1.2	0.24	0.72

Table 2. The parameters used in our calculations.

are still relevant as such rounding of the corners is present in experiments including that of Downs & Fransson (2014).

Finally, the third form of roughness arrays considered comprises a streamwise step-like geometry and a spanwise sinusoidal shape, which is defined as

$$F_f(x) = \frac{1}{2}\left[\tanh\left(\frac{x-1+l_x}{d_x}\right) - \tanh\left(\frac{x-1-l_x}{d_x}\right)\right], \quad F_g(Z) = \frac{1}{2}\cos(\beta Z). \quad (4.4)$$

This case is included in order to contrast the stability properties of different configurations. The parameters characterising the streamwise distribution are the same as those in the second configuration. The above three cases are referred to as Roughness 1, 2 and 3, respectively.

5. Numerical results for the roughness-induced streaky flow

For Roughness 1 (4.1) with a given d, the streaky flow induced is controlled by the height h and the spanwise wavenumber β. Numerical results indicate that the strength of the streaks increases monotonically with h or β when the other parameter d is fixed. For different values of h or β, the strength of the streaks, the spanwise distribution of the velocity U and the wall shear in the Z/Λ coordinate system remain nearly the same when the product $h\beta$ is the same. Downstream of the roughness array region, boundary-layer separation of collision type may occur, whose position depends on the height h for a given β. The boundary-layer solution cannot be continued beyond the separation point. In the present study, the maximum streak strength is calculated for the parameter $h\beta = 0.05\pi$, and separation takes place near $x = 1.5$. For larger values of $h\beta$, the position shifts upstream. This phenomenon was observed earlier in the numerical results of Kátai & Wu (2020) and Zheng & Wu (2024).

The flow evolution remains similar for streaks of different strengths. For brevity, numerical results of the streaky flow are presented for only one case with parameters $h = 0.11$ and $\beta = 0.455\pi$. However, in the stability analysis, we also examined other streaky flows.

5.1. *Inviscid-deck solution*

As was shown earlier, the solution in the inviscid deck provides the values of w and p_Z at the 'boundary surface', which represent the spanwise slip velocity and surface pressure gradient, respectively, and they drive the streaky boundary-layer flow, as is indicated by matching conditions (3.16*b*) and spanwise momentum (2.3*c*). Contours of these quantities on the (x, Z) plane are displayed in figure 2, indicating that w and p_Z on the surface are antisymmetric about $Z/\Lambda = 0$. Downstream of the peak ($x > 1$), the positive and negative signs of the spanwise velocity and pressure gradient for $Z/\Lambda < 0$ and $Z/\Lambda > 0$, respectively, mean that the fluid is brought towards the plane $Z/\Lambda = 0$, and an 'adverse pressure gradient' is present on either side of $Z/\Lambda = 0$. As a result, a collision type of separation arises as is shown later. Interestingly, the spanwise surface pressure gradient

https://doi.org/10.1017/jfm.2026.11174 Published online by Cambridge University Press

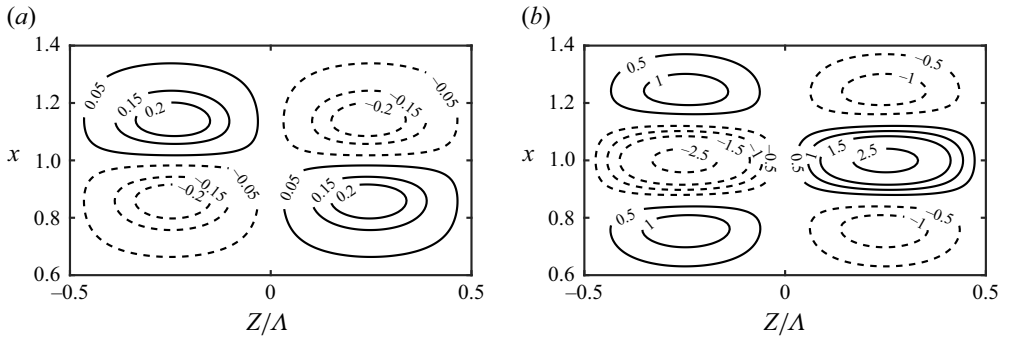


Figure 2. Contours of (*a*) the spanwise slip velocity w and (*b*) the spanwise surface pressure gradient p_Z for $h = 0.11$, $d = 0.2$ and $\beta = 0.455\pi$.

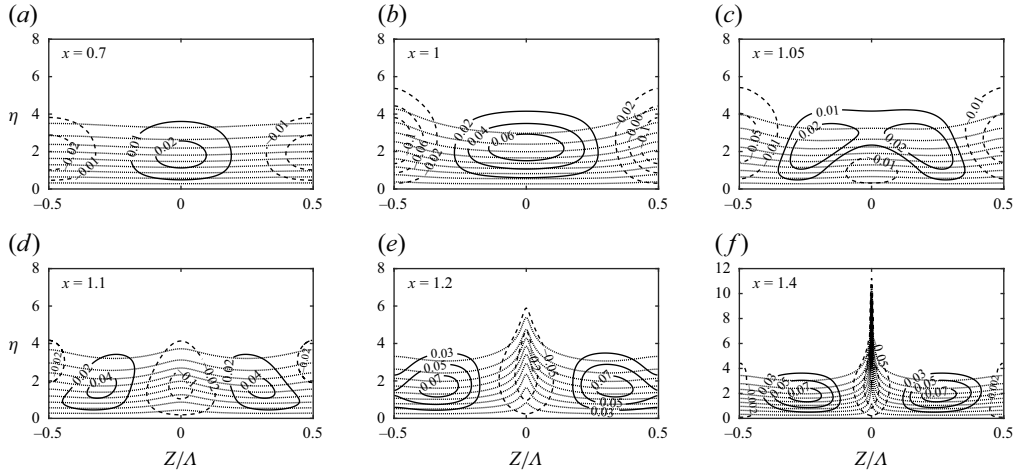


Figure 3. Contours of the streaky flow at (*a–f*) different streamwise positions for $h = 0.11$, $d = 0.2$ and $\beta = 0.455\pi$. Curves: solid, $U_1 > 0$; dashed, $U_1 < 0$; dotted, $U = U_B + U_1$.

and slip velocity also exhibit approximate symmetry and antisymmetry about $x = 1$, respectively, which is due to the fact that the roughness element shape is approximately symmetric about $x = 1$.

5.2. *Streaky boundary-layer flow*

The spanwise-periodic roughness arrays cause the initially 2-D background (Blasius) flow to become a 3-D streaky flow, the formation and streamwise evolution of which are illustrated by contours of the roughness-induced streamwise velocity displayed in figure 3. Upstream of the peak ($x < 1$), low-speed streaks emerge around $Z/\Lambda = \pm 1/2$, while a high-speed streak forms along $Z/\Lambda = 0$ near the wall. From $x = 1$ to 1.1, the high-speed region 'elongates' in the spanwise direction and splits into two, which outflanks a faint low-speed streak that forms in between. From $x = 1.1$ to 1.2, the low- and high-speed streaks intensify. Downstream of $x = 1.2$, the central low-speed streak concentrates in the spanwise direction and is lifted up in the wall-normal direction, so that a cusp starts to form in the contours. This feature suggests that a collision type of boundary-layer separation is imminent downstream. With the streamwise pressure gradient absent, the separation is caused by the 'adverse' spanwise pressure gradient on either side of $Z = 0$, probably

https://doi.org/10.1017/jfm.2026.11174 Published online by Cambridge University Press

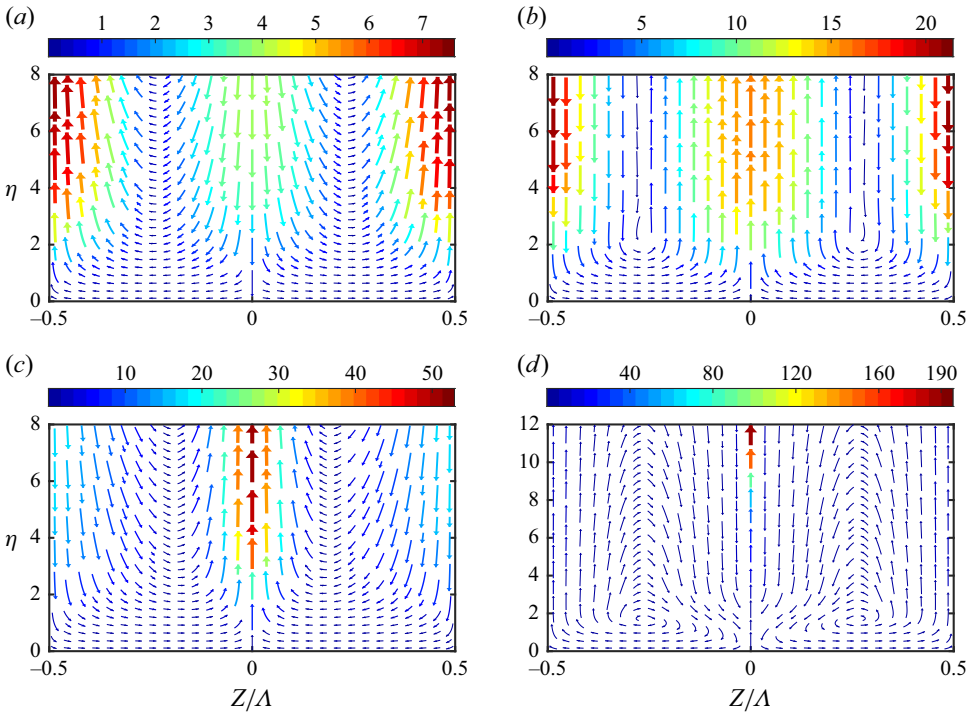


Figure 4. Velocity vectors in the cross-flow plane at (*a*) $x = 0.7$, (*b*) $x = 1$, (*c*) $x = 1.1$ and (*d*) $x = 1.4$. The colours represent the modulus of the velocity vector.

similar to that described in Stewartson & Simpson (1982) and Goldstein & Leib (1993). The cusp signals shortening of the spanwise length scale and formation of a singularity of focusing kind. The present classical boundary-layer equations cannot describe the flow in the separation region. This is the limitation of the present theory. A detailed analysis of the separation region is required to identify first the singularity structure as well as the physical mechanism that may remove the singularity, and then develop the theory capable of describing the separated flow. This task is beyond the scope of the present study, but we consider it an important topic for future investigation. Our view is that the singularity is likely to be resolved by a local asymptotic theory that accounts for full spanwise diffusion or ellipticity, and it follows that the flow upstream of the separation would not deviate significantly from the results obtained by marching. This viewpoint is supported by the fact that solutions to the boundary-region equations remain regular despite these equations being parabolic in the streamwise direction (Goldstein *et al.* 2016; Xu, Zhang & Wu 2017). Figure 4 shows the velocity vectors (V, W) in the cross-flow plane at the streamwise positions corresponding to those in figure 3. The high-speed streaks along $Z/\Lambda = 0$ upstream ($x < 1$) are associated with the downward motion on both sides. This switches to upwash in the region downstream ($x > 1$), leading to formation of the low-speed streak. This reversal of the cross-flow velocity is a direct consequence of hF_x, which controls the spanwise slip velocity and pressure gradient as was noted in § 3.1. The change of the sign of f_x at the peak position ($x = 1$) leads to the switchover from downwash to upwash.

The streak amplitude and the boundary-layer thickness are two important physical quantities of the streaky flow. The former is defined using the integral streak amplitude

https://doi.org/10.1017/jfm.2026.11174 Published online by Cambridge University Press

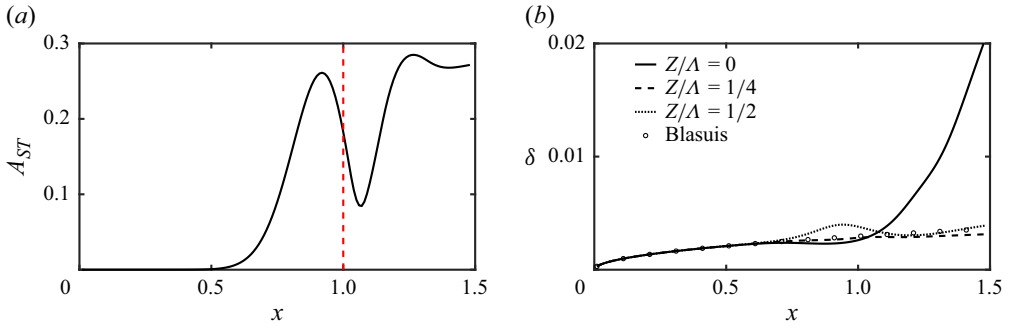


Figure 5. The streamwise development of (*a*) the streak amplitude A_{ST} and (*b*) the non-dimensional displacement thickness δ for $h = 0.11$, $d = 0.2$, $\beta = 0.455\pi$ and $\epsilon = 0.2036$.

as (Shahinfar *et al.* 2013)

$$A_{ST}(x) = \frac{1}{\Lambda}\int_{-\Lambda/2}^{\Lambda/2}\int_{0}^{\infty}\left|U(x,\eta,Z) - U^{Z}(x,\eta)\right| \mathrm{d}\eta\,\mathrm{d}Z, \tag{5.1}$$

where the superscript 'Z' denotes a spanwise-averaged quantity, while the latter is taken to be the dimensionless displacement thickness δ, defined as

$$\delta(x,Z) = \int_{h^*F}^{\infty}\left[1 - U(x^*,y^*,z^*)\right]\,\mathrm{d}y^* = Re^{-1/2}x^{1/2}\int_{0}^{\infty}\left[1 - U(x,\eta,Z)\right]\,\mathrm{d}\eta. \tag{5.2}$$

Figure 5(*a*) shows the streak amplitude versus x. Interestingly, A_{ST} does not follow the simple trend of monotonic increase–decrease of the roughness height. Instead, two local maxima form at $x = 0.92$ and 1.27, which are upstream and downstream of the roughness-array peak ($x = 1$), respectively, while close to the peak height, a local minimum occurs at $x = 1.07$. Further downstream of the roughness elements, the spanwise pressure gradient gradually diminishes but the streak amplitude changes slowly, implying that streaks may persist over a distance much longer than do the roughness arrays. Figure 5(*b*) shows the streamwise evolution of the displacement thickness along $Z/\Lambda = 0$, 1/4 and 1/2, together with the result of the Blasius solution. Upstream of $x = 1.07$, the largest displacement thickness is found along $Z/\Lambda = 1/2$, where the distortion concentrates, while the displacement thickness hardly alters along $Z/\Lambda = 0$. In contrast, downstream of $x = 1.07$, the largest displacement thickness is observed along $Z/\Lambda = 0$. This is intrinsically associated with collision-type separation, signalled by the formation of the cusp, shown in figure 3.

Similar to previous studies (Kátai & Wu 2020; Zhu & Wu 2022; Zheng & Wu 2024), the wall shear controls the lower-branch viscous instability at leading order, but the latter is now also influenced by the shape of the roughness arrays. Figure 6 shows contours of the total wall shear $\lambda_u(x,Z) = \partial U/\partial Y(x,0,Z)$ and the deviation from the Blasius flow, $\Delta\lambda_u(x,Z) = \partial U_1/\partial Y(x,0,Z)$. Upstream of the peak, a maximum is observed in the central region, with a minimum on either side. Downstream of the peak, the minimum occurs along the centreline ($Z/\Lambda = 0$), while the maximum appears around $Z/\Lambda = \pm 1/4$.

The characteristics of the wall shear are further analysed in the supplementary material available at https://doi.org/10.1017/jfm.2026.11174, where λ_u is found to undergo spanwise concentration towards $Z/\Lambda = 0$. The development of the Fourier spectral components of λ_u indicates that even though only the fundamental component is present in the roughness shape function, harmonics are generated downstream in λ_u due to nonlinear effects,

https://doi.org/10.1017/jfm.2026.11174 Published online by Cambridge University Press

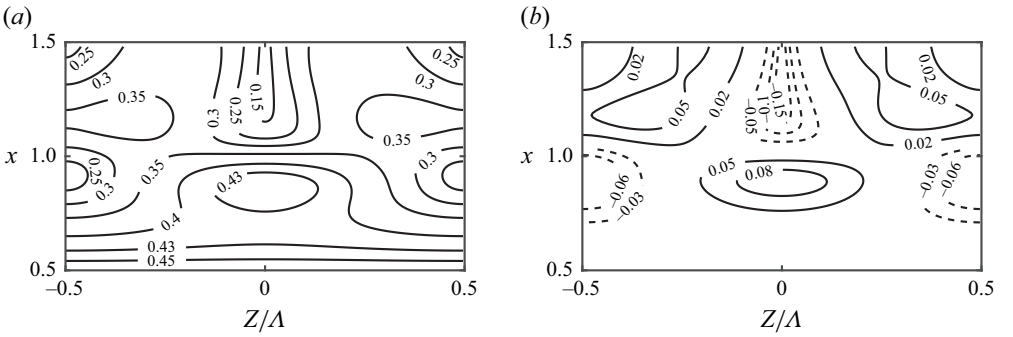


Figure 6. Contours of (*a*) the total wall shear $\lambda_u(x, Z) = \partial U/\partial Y(x, 0, Z)$ and (*b*) the streak-associated wall shear $\Delta\lambda_u(x, Z) = \partial U_1/\partial Y(x, 0, Z)$, on the (x, Z) plane for $h = 0.11$, $d = 0.2$ and $\beta = 0.455\pi$.

and higher harmonics eventually gain greater amplitudes causing spanwise focusing and eventual separation of collision type.

6. Linear stability analysis of the streaky boundary layer

In the absence of roughness elements, the lower-branch TS instability is governed by the standard triple-deck structure (Lin 1946; Smith 1979*a*). The characteristic frequency and wavelength of the instability modes are of $O(\epsilon^{-2})$ and $O(\epsilon^3)$, respectively, and they remain applicable in the presence of roughness elements, as was shown in Kátai & Wu (2020). It is therefore convenient to introduce the rescaled time variable and spatial coordinates:

$$t = \epsilon^{-2}t^* = O(1), \quad X = \epsilon^{-3}x^* = O(1). \tag{6.1a,b}$$

6.1. *Lower deck*

The lower deck of the viscous instability is a very thin layer adjacent to the curved surface with an $O(\epsilon^5)$ width. Thus the local wall-normal coordinate is introduced as

$$\bar{Y} = \epsilon^{-5}(y^* - h^*F) = O(1). \tag{6.2}$$

The flow is decomposed into the streaky base flow and a small-amplitude disturbance, namely

$$\begin{aligned}(u^*, v^*, w^*, p^*) = (\bar{U}_b, \epsilon^4\bar{V}_b, \epsilon^3\bar{W}_b, \epsilon^6\bar{P}_b)\\ + \epsilon_d(\epsilon\bar{U}_d, \epsilon^3\bar{V}_d + \epsilon h F_Z\bar{W}_d, \epsilon\bar{W}_d, \epsilon^2\bar{P}_d)E + \text{c.c.},\end{aligned} \tag{6.3}$$

where the subscripts 'b' and 'd' denote the streaky base flow and the disturbance, respectively, and 'c.c.' stands for complex conjugate. The disturbance has a small amplitude $\epsilon_d \ll 1$ and is of modal form proportional to $E = \exp[\mathrm{i}\alpha X - \mathrm{i}\omega t]$, where $\alpha = O(1)$ and $\omega = O(1)$ are the normalised wavenumber and frequency, respectively.

The lower deck for the instability mode with an $O(\epsilon^5)$ thickness is much thinner than the streaky boundary layer, whose thickness is of $O(\epsilon^4)$. Therefore, we approximate the base-flow velocities by their Taylor series expansions about the wall:

$$\bar{U}_b = \epsilon\lambda_u\bar{Y} + \cdots, \quad \bar{V}_b = \epsilon^2\lambda_v\bar{Y}^2 + \cdots, \quad \bar{W}_b = \epsilon\lambda_w\bar{Y} + \cdots, \tag{6.4a–c}$$

where λ_u and λ_w are the streamwise and spanwise wall shears, respectively, and $\lambda_v = -(\partial\lambda_u/\partial x + \partial\lambda_w/\partial Z)/2$. Substituting (6.1), (6.3) and (6.4) along with (2.1*c*) into the NS

https://doi.org/10.1017/jfm.2026.11174 Published online by Cambridge University Press

equations and linearising, we obtain the lower-deck disturbance equations:

$$\mathrm{i}\alpha\bar{U}_d + \frac{\partial\bar{V}_d}{\partial\bar{Y}} + \frac{\partial\bar{W}_d}{\partial Z} = 0, \tag{6.5a}$$

$$(\mathrm{i}\alpha\lambda_u\bar{Y} - \mathrm{i}\omega)\bar{U}_d + \lambda_u\bar{V}_d + \lambda_{uZ}\bar{Y}\bar{W}_d = -\mathrm{i}\alpha\bar{P}_d + (1+h^2F_Z^2)\frac{\partial^2\bar{U}_d}{\partial\bar{Y}^2}, \tag{6.5b}$$

$$(\mathrm{i}\alpha\lambda_u\bar{Y} - \mathrm{i}\omega)\bar{W}_d = -\frac{\partial\bar{P}_d}{\partial Z} + (1+h^2F_Z^2)\frac{\partial^2\bar{W}_d}{\partial\bar{Y}^2}, \tag{6.5c}$$

along with $\partial\bar{P}_d/\partial\bar{Y} = 0$. The non-parallelism associated with the slow variable, $\partial/\partial X$, is of $O(\epsilon^3)$ and thus negligible in the disturbance momentum equations at leading order for the elongated roughness elements. Given that the wall-normal length scale in the lower deck is much smaller than the streamwise and spanwise length scales, the wall-normal diffusion is a leading-order effect, as usual, but as with the streaky base flow the spanwise diffusion plays a leading role in the streamwise and spanwise momentum equations through the coordinate shift (6.2); $\partial^2(\bar{U}_d, \bar{W}_d)/\partial z^{*2}$ together with (6.2) contributes to the extra terms $\partial^2(\bar{U}_d, \bar{W}_d)/\partial\bar{Y}^2$ in (6.5*b*) and (6.5*c*). As a result, the coefficients of the viscous terms are modified to $1+h^2F_Z^2$. This geometric effect arises due to the roughness arrays having an $O(1)$ spanwise slope, and its presence stands as a main difference from the previous work (Kátai & Wu 2020; Zheng & Wu 2024).

6.2. *Main-deck solution*

In the main deck, where the shifted coordinate $Y = O(1)$, the velocities and pressure expand as

$$\begin{aligned}(u^*, v^*, w^*, p^*) = {} & (U_b, \epsilon^4 V_b, \epsilon^3 W_b, \epsilon^6 P_b) \\ & + \epsilon_d\Big(\epsilon U_d, \epsilon^2(V_d + hF_Z W_d), \epsilon^2 W_d, \epsilon^2 P_d\Big)E + \text{c.c.}\end{aligned} \tag{6.6}$$

Note that Prandtl's transformation is applied as indicated by the expression for the wall-normal velocity of the disturbance. Substitution of (6.1), (6.6) and (2.1*b*,*c*) into the NS equations leads to the leading-order equations for the disturbance in the main deck:

$$\mathrm{i}\alpha U_d + \frac{\partial V_d}{\partial Y} = 0, \quad \mathrm{i}\alpha U_b U_d + V_d\frac{\partial U_b}{\partial Y} = 0, \quad \mathrm{i}\alpha U_b W_d + \frac{\partial P_d}{\partial Z} = 0, \tag{6.7a–c}$$

plus $\partial P_d/\partial Y = 0$. The solution is found as

$$U_d = A_1\frac{\partial U_b}{\partial Y}, \quad V_d = -\mathrm{i}\alpha A_1 U_b, \quad W_d = -\frac{1}{\mathrm{i}\alpha U_b}\frac{\partial P_d}{\partial Z}, \quad P_d = \bar{P}_d(Z), \tag{6.8a–d}$$

where $A_1(X, Z)$ is the displacement function. Note that in terms of the shifted coordinate (2.1*b*) and transformed V_d, the solution remains of the same form as that in the flat-plate case.

6.3. *Upper-deck analysis*

In the upper deck, the velocities and pressure expand as

$$(u^*, v^*, w^*, p^*) = (1, \epsilon^3 v_b, \epsilon^3 w_b, \epsilon^6 p_b) + \epsilon_d\epsilon^2(u_d, v_d, w_d, p_d)E + \text{c.c.} \tag{6.9}$$

Substituting (6.1), (6.9) and $y = \epsilon^{-3}y^*$ into the NS equations, we obtain

$$\mathrm{i}\alpha u_d + \frac{\partial v_d}{\partial y} + \frac{\partial w_d}{\partial Z} = 0, \quad u_d = -p_d, \quad \mathrm{i}\alpha v_d = -\frac{\partial p_d}{\partial y}, \quad \mathrm{i}\alpha w_d = -\frac{\partial p_d}{\partial Z}, \tag{6.10a–d}$$

https://doi.org/10.1017/jfm.2026.11174 Published online by Cambridge University Press

which can be rearranged into a single equation for p_d:

$$-\alpha^2 p_d + \frac{\partial^2 p_d}{\partial y^2} + \frac{\partial^2 p_d}{\partial Z^2} = 0. \tag{6.11}$$

The matching conditions read

$$\left.\frac{\partial p_d}{\partial y}\right|_{y\to hF} \to -\alpha^2 A_1 + hF_Z \frac{\partial P_d}{\partial Z}, \quad p_d|_{y\to hF} \to P_d(Z), \tag{6.12a,b}$$

where the first condition follows from (6.10*c*) and matching the wall-normal and spanwise velocities in the upper deck, v_d and w_d, with their main-deck counterparts given in (6.6) and (6.8*b*,*c*).

Somewhat surprisingly, the roughness arrays affect the streaky flow and its instability in different manners. Roughness arrays displace streamlines to induce a pressure and a spanwise slip velocity, which act on the boundary layer, driving a spanwise motion. The latter then generates streaks. The relation between the steady perturbations in the main and outer layers is 'hierarchical'. In contrast, for the instability, the relation is an interactive one: the wall-normal and spanwise velocities of the mode in the main layer affect the pressure generation in the upper layer. The pressure in turn drives the mode in the lower deck.

6.4. *The lower-deck solutions*

The lower-deck disturbance equations are solved following similar steps in Smith (1979*b*), Walton (1996) and Walton & Patel (1998). We introduce the rescaled variable

$$\zeta = (1 + h^2 F_Z^2)^{-1/3} (\mathrm{i}\lambda_u \alpha)^{1/3} \bar{Y} + \zeta_0, \tag{6.13}$$

where $\zeta_0 = -\mathrm{i}\omega(1 + h^2 F_Z^2)^{-1/3}(\mathrm{i}\lambda_u\alpha)^{-2/3}$.

Rewritten in terms of ζ, the spanwise momentum (6.5*c*) is simplified to

$$\frac{\partial^2 \bar{W}_d}{\partial \zeta^2} - \zeta \bar{W}_d = (1 + h^2 F_Z^2)^{-1/3} (\mathrm{i}\lambda_u \alpha)^{-2/3} \frac{\partial \bar{P}_d}{\partial Z}, \tag{6.14}$$

which satisfies the no-slip and matching conditions:

$$\bar{W}_d = 0 \quad \text{at} \quad \zeta = \zeta_0; \quad \bar{W}_d \to -(1 + h^2 F_Z^2)^{-1/3} (\mathrm{i}\lambda_u \alpha)^{-2/3} \zeta^{-1} \frac{\partial \bar{P}_d}{\partial Z} \quad \text{as} \quad \zeta \to \infty. \tag{6.15a,b}$$

The solution to (6.14)–(6.15) is given by

$$\bar{W}_d = \pi \left(1 + h^2 F_Z^2\right)^{-1/3} (\mathrm{i}\lambda_u \alpha)^{-2/3} \frac{\partial \bar{P}_d}{\partial Z} \left[\frac{\mathrm{Gi}(\zeta_0)}{\mathrm{Ai}(\zeta_0)} \mathrm{Ai}(\zeta) - \mathrm{Gi}(\zeta)\right]. \tag{6.16}$$

Differentiating (6.5*b*) with respect to $\bar{Y}$ to eliminate the pressure and using (6.5*a*) to eliminate $\bar{V}_d$ in the resulting equation, we obtain the equation governing $\bar{U}_d$:

$$(\mathrm{i}\alpha\lambda_u \bar{Y} - \mathrm{i}\omega) \frac{\partial \bar{U}_d}{\partial \bar{Y}} - \lambda_u \frac{\partial \bar{W}_d}{\partial Z} + \lambda_{uZ} \bar{W}_d + \lambda_{uZ} \bar{Y} \frac{\partial \bar{W}_d}{\partial \bar{Y}} = \left(1 + h^2 F_Z^2\right) \frac{\partial^3 \bar{U}_d}{\partial \bar{Y}^3}. \tag{6.17}$$

In order to solve for $\bar{U}_d$, (6.17) is rewritten in terms of ζ as

$$\frac{\partial^3 \bar{U}_d}{\partial \zeta^3} - \zeta \frac{\partial \bar{U}_d}{\partial \zeta} = -\frac{1}{\mathrm{i}\alpha} \frac{\partial \bar{W}_d}{\partial Z} + \frac{\lambda_{uZ}}{\mathrm{i}\alpha\lambda_u} \bar{W}_d + (\zeta - \zeta_0) \frac{\lambda_{uZ}}{\mathrm{i}\alpha\lambda_u} \frac{\partial \bar{W}_d}{\partial \zeta}, \tag{6.18}$$

https://doi.org/10.1017/jfm.2026.11174 Published online by Cambridge University Press

on which the boundary and matching conditions are specified as

$$\bar{U}_d = 0, \quad \frac{\partial^2 \bar{U}_d}{\partial \zeta^2} = \left(1 + h^2 F_Z^2\right)^{-1/3} (\mathrm{i}\lambda_u \alpha)^{-2/3} \mathrm{i}\alpha \bar{P}_d \quad \text{at} \ \ \zeta = \zeta_0; \tag{6.19a,b}$$

$$\bar{U}_d \to \lambda_u A_1 \quad \text{as} \ \ \zeta \to \infty. \tag{6.19c}$$

The solution to (6.18)–(6.19) is found as

$$\begin{aligned}\bar{U}_d(\zeta) = & D_0 \int_{\zeta_0}^{\zeta} \mathrm{Ai}(\tau)\mathrm{d}\tau + \left(D_1 - \frac{3}{4} D_3\right) [\mathrm{Ai}(\zeta) - \mathrm{Ai}(\zeta_0)] + \frac{D_3}{4} \left[\zeta \mathrm{Ai}'(\zeta) - \zeta_0 \mathrm{Ai}'(\zeta_0)\right] \\ & + \left(D_2 - \frac{3}{4} D_4\right) [\mathrm{Gi}(\zeta) - \mathrm{Gi}(\zeta_0)] + \frac{D_4}{4} \left[\zeta \mathrm{Gi}'(\zeta) - \zeta_0 \mathrm{Gi}'(\zeta_0)\right], \end{aligned} \tag{6.20}$$

where the expressions for D_j $(j = 0, 1, 2, 3, 4)$ are given in Appendix B.

Imposing (6.19*c*) on (6.20) leads to the pressure equation:

$$\frac{\partial^2 \bar{P}_d}{\partial Z^2} - K_1 \frac{\partial \bar{P}_d}{\partial Z} - \alpha^2 \bar{P}_d = K_2 A_1, \tag{6.21}$$

where

$$K_1 = \left[\mathrm{Ai}'(\zeta_0) + \zeta_0 \kappa(\zeta_0)\right] \frac{\zeta_0}{2\mathrm{Ai}(\zeta_0)} \left[\frac{\lambda_{uZ}}{\lambda_u} + \frac{h^2 F_Z F_{ZZ}}{1 + h^2 F_Z^2}\right] + \frac{3}{2} \frac{\lambda_{uZ}}{\lambda_u} + \frac{h^2 F_Z F_{ZZ}}{2\left(1 + h^2 F_Z^2\right)}, \tag{6.22a}$$

$$K_2 = \left(1 + h^2 F_Z^2\right)^{1/3} (\mathrm{i}\lambda_u \alpha)^{5/3} \mathrm{Ai}'(\zeta_0) \kappa(\zeta_0)^{-1}, \quad \kappa(\zeta_0) = \int_{\zeta_0}^{\infty} \mathrm{Ai}(\tau)\mathrm{d}\tau, \tag{6.22b,c}$$

with $\mathrm{Ai}(\zeta)$ and $\mathrm{Gi}(\zeta)$ denoting the Airy and Scorer functions, respectively. A closed system describing the viscous lower-branch instability is formed by (6.11), (6.12) and (6.21). In contrast to bi-global stability analysis (Piot *et al.* 2008; Siconolfi *et al.* 2015; Szabó *et al.* 2024; Bi *et al.* 2023), the asymptotically reduced system is a one-dimensional eigenvalue problem in the spanwise direction. The coefficients in (6.21) depend solely on λ_u, hF and their spanwise derivatives, which provides *a priori* insight that the viscous lower-branch instability is controlled at leading order by the spanwise-dependent wall shear and the shape function of the roughness elements. The latter is an added new feature compared with Kátai & Wu (2020), arising due to longer and higher roughness elements being considered.

6.5. *The eigenvalue problem*

Given that $F_Z(x, Z)$ and the streaky base flow $U(x, Y, Z)$ are spanwise-periodic, so are the coefficients K_1 and K_2 in (6.21). Thus, we adopt Floquet theory to solve the one-dimensional eigenvalue problem, expressing p_d, $\bar{P}_d$ and A_1 as

$$(p_d, \bar{P}_d, A_1) = \exp(\mathrm{i}q\beta Z) \sum_{n=-\infty}^{\infty} (\bar{p}_n(y), \bar{P}_n, \bar{A}_n) \exp(\mathrm{i}n\beta Z), \tag{6.23}$$

where q is the Floquet exponent, restricted to the interval $[0, 1/2]$ as explained by Kátai & Wu (2020). Substitution of (6.23) into (6.11) yields

$$\frac{\partial^2 \bar{p}_n}{\partial y^2} - \left[(n + q)^2 \beta^2 + \alpha^2\right] \bar{p}_n = 0. \tag{6.24}$$

https://doi.org/10.1017/jfm.2026.11174 Published online by Cambridge University Press

The solution satisfying the attenuating far-field condition for $\bar{p}_n$ is

$$\bar{p}_n(y) = C_n \exp\Big[-\sqrt{(n+q)^2\beta^2+\alpha^2}\,y\Big], \tag{6.25}$$

where C_n is a coefficient. Substituting (6.23) with (6.25) into (6.12) and writing the resulting equation in terms of $\bar{y}$ lead to

$$\bar{P}_n = \sum_{k=-\infty}^{\infty} a_{nk} C_k, \tag{6.26a}$$

$$\bar{A}_n = \sum_{k=-\infty}^{\infty} \alpha^{-2}\Big[\sqrt{(k+q)^2\beta^2+\alpha^2}(a_{nk}+c_{nk}) - \mathrm{i}(k+q)\beta b_{nk}\Big]C_k, \tag{6.26b}$$

where we have performed Fourier series expansions:

$$\big(1, hF_Z, h^2F_Z^2\big)\exp\Big[-\sqrt{(k+q)^2\beta^2+\alpha^2}hF\Big]\exp(\mathrm{i}k\beta Z) = \sum_{n=-\infty}^{\infty}(a_{nk}, b_{nk}, c_{nk})\mathrm{e}^{\mathrm{i}n\beta Z}. \tag{6.27}$$

Similarly, we rewrite K_1 and K_2 into Fourier series:

$$K_1 = \sum_{l=-\infty}^{\infty} R_l \mathrm{e}^{\mathrm{i}\beta l Z}, \quad K_2 = \sum_{l=-\infty}^{\infty} Q_l \mathrm{e}^{\mathrm{i}\beta l Z}. \tag{6.28a,b}$$

Substituting (6.26) with (6.28) into (6.21) and equating the coefficients of the respective Fourier components, we arrive at the equations

$$\big[\alpha^2+\beta^2(n+q)^2\big]\bar{P}_n = -\sum_{j=-\infty}^{\infty}\mathrm{i}\beta(j+q)R_{n-j}\bar{P}_j - \sum_{j=-\infty}^{\infty} Q_{n-j}\bar{A}_j. \tag{6.29}$$

Truncating the system (6.29) for $-K \leqslant n \leqslant K$ and eliminating $\bar{A}_j$ using (6.26), we write (6.29) in matrix form:

$$\boldsymbol{M}\bar{\boldsymbol{P}} = 0, \tag{6.30}$$

where $\bar{\boldsymbol{P}} = (\bar{P}_{-K}, \bar{P}_{-K+1}, \ldots, \bar{P}_0, \ldots, \bar{P}_K)^T$. The implicit dispersion relation is given by

$$\mathcal{D}(\alpha) \equiv \det\big(\boldsymbol{M}(\alpha, \omega, \lambda_u, q, hF)\big) = 0. \tag{6.31}$$

In the absence of roughness arrays, the dispersion relation (6.31) degenerates into

$$D_B(\alpha) \equiv \alpha^2\big[\alpha^2+\beta^2(n+q)^2\big]^{1/2} + (\mathrm{i}\alpha\lambda_B(x))^{5/3}\mathrm{Ai}'(\zeta_0)\kappa(\zeta_0)^{-1} = 0, \tag{6.32}$$

where $\beta_{TS} = \beta(n+q)$ is the spanwise wavenumber of TS modes and $\lambda_B(x)$ represents the wall shear of the Blasius flow.

We focus on the spatial instability for which the frequency ω is real, and $\alpha = \alpha_r + \mathrm{i}\alpha_i$ is complex with α_r being the streamwise wavenumber and $-\alpha_i$ the growth rate. The implicit dispersion relation (6.31) is solved using Muller's iteration method (Muller 1956). The numerical program used for these calculations is an in-house code that has been validated in previous studies (Kátai & Wu 2020; Zhu & Wu 2022; Zheng & Wu 2024). Furthermore, computations with different values of K ensure that numerical results are independent of K.

https://doi.org/10.1017/jfm.2026.11174 Published online by Cambridge University Press

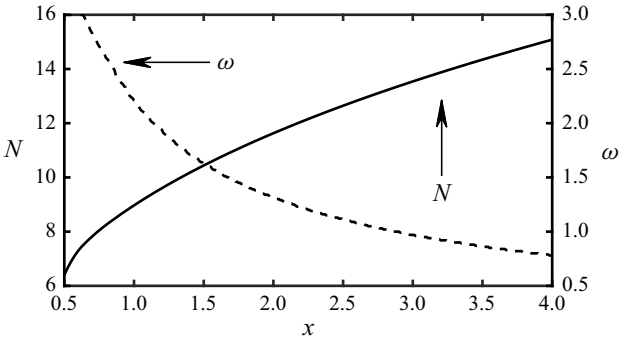


Figure 7. Streamwise variation of the N-factor (solid line) in the flat-plate case for $\beta_{TS} = 0$ and the corresponding frequency (dashed line) of the most amplified mode.

Given that sufficiently upstream of the roughness arrays the base flow approaches the state of the flat-plate case, the solutions for (6.31) and (6.32) are the same there. The latter may thus be used as the an initial guess to initiate the iteration for finding the former. A mode in the primary region influenced by roughness can be considered as developing continuously from a usual TS mode, and is computed as such. Detailed descriptions of the solution procedure and physical interpretation can be found in Kátai & Wu (2020).

7. Numerical results for the stability problem

7.1. *Local growth rates*

In order to investigate the influence of the roughness elements on the TS modes, we first determine the most relevant ones on which to focus. Transition is related to the accumulated growth of disturbances, which is, in the linear regime, measured by the N-factor, defined as

$$N(\omega, \beta_{TS}) = -\epsilon^{-3} \int_{x_n}^{x} \alpha_i(x)\, \mathrm{d}x, \tag{7.1}$$

where x_n denotes the neutral position, i.e. $\alpha_i(x_n) = 0$. In the incompressible regime, the most unstable and most amplified modes are 2-D. To select appropriate upstream modes to trace, we calculate the local growth rate and N-factors of 2-D TS modes ($\beta_{TS} = 0$) in the case of a flat plate. Figure 7 shows the streamwise variation of the N-factor and the corresponding frequency of the most amplified mode, i.e. the mode with the largest N at location x. The N-factor and the corresponding frequency ω increase and decrease with x, respectively. The results indicate that modes with frequency $\omega \in [0.5, 3]$ acquire large N-factors (while modes outside this frequency band would either acquire large N-factors at too distant locations downstream or have considerably smaller N-factors). Based on this observation, we investigate effects of roughness elements on the TS modes with frequencies ranging from 0.5 to 3.

Figure 8 displays the local growth rates for roughness arrays with the same spanwise wavenumber $\beta = 0.455\pi$ but different heights, $h = 0.095$ and 0.11. The first, second and third columns are pertinent to streamwise locations $x = 0.9$, 1.2 and 1.4, respectively. The TS modes with spanwise wavenumbers $\beta_{TS} = 0$, 0.1π and 0.2π are computed. The non-zero values of β_{TS} cover a substantial range of obliqueness angles; e.g. at $x = 0.9$, $\beta_{TS} = 0.2\pi$ covers obliqueness angles between 35° (minimum) and 74° (maximum), which are attained by modes with $\omega = 0.5$ and 3, respectively. The first and second rows in

https://doi.org/10.1017/jfm.2026.11174 Published online by Cambridge University Press

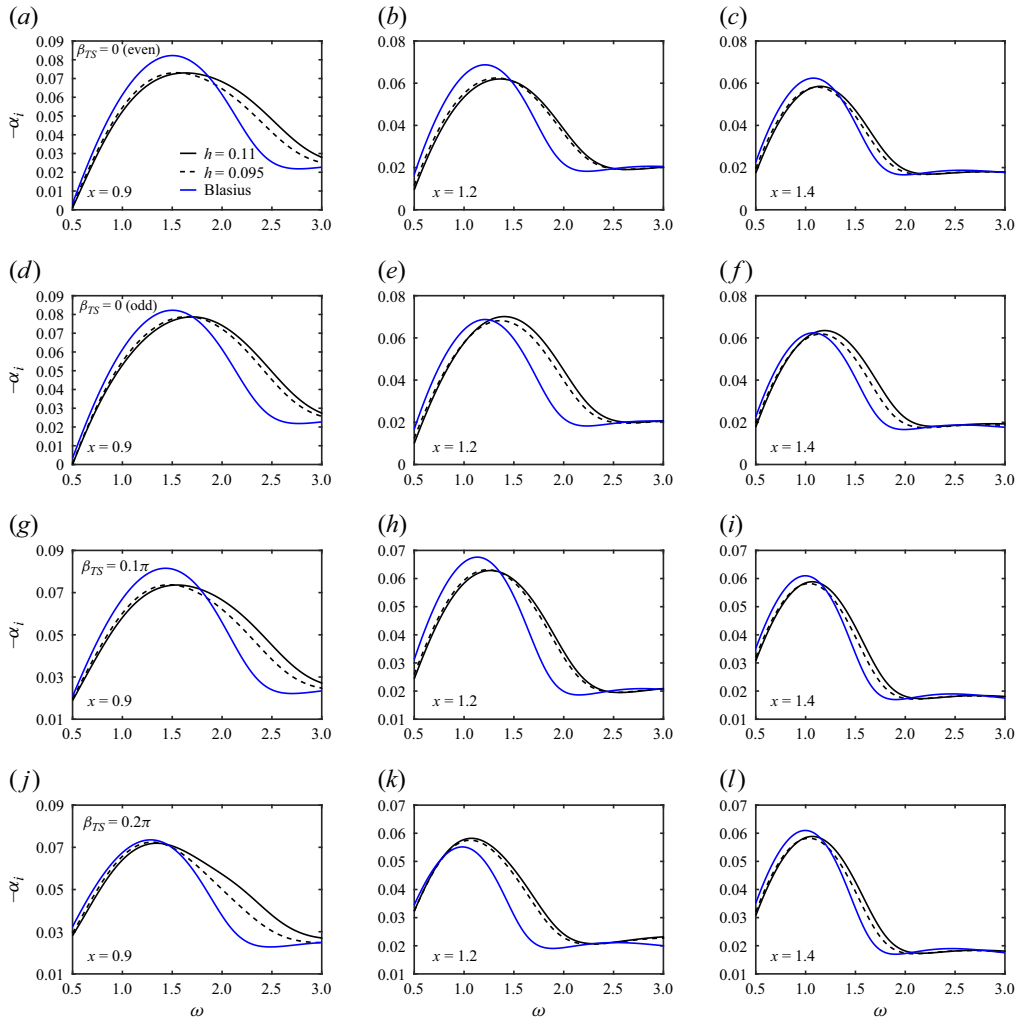


Figure 8. Local growth rates ($-\alpha_i$) versus the frequency ω of planar ($\beta_{TS} = 0$) and oblique modes at various streamwise positions. (*a–c*) Symmetric (even) modes; (*d–f*) antisymmetric (odd) modes; (*g–i*) $\beta_{TS} = 0.1\pi$; (*j–l*) $\beta_{TS} = 0.2\pi$. Curves: blue solid, Blasius; black solid, $h = 0.11$; black dashed, $h = 0.095$. For both heights, the arrays have spanwise wavenumber $\beta = 0.455\pi$.

figure 8 show the results for the 2-D modes ($\beta_{TS} = 0$), which are unique in that their ensuing development may be either symmetric or antisymmetric; they will, for brevity, be referred to as 'even' and 'odd' modes, respectively. Clearly, low-frequency modes are stabilised by the roughness elements, while higher-frequency modes are destabilised, consistent with the finding in Kátai & Wu (2020). Even and odd modes follow similar trends across the frequency range with odd modes having slightly higher growth rates (cf. figures 8*a–c* and 8*d–f*). The 'critical' frequency for the switching from stabilising to destabilising effects depends on the streamwise location and weakly on the value of h. The above conclusions hold for weakly oblique TS modes, as is indicated in the third row of figure 8 for $\beta_{TS} = 0.1\pi$. For stronger 3-D modes, the stabilising effect on low-frequency modes becomes weaker, whereas the destabilising effect extends to lower frequencies and becomes more significant as the fourth row in figure 8 shows. A comparison of the results

https://doi.org/10.1017/jfm.2026.11174 Published online by Cambridge University Press

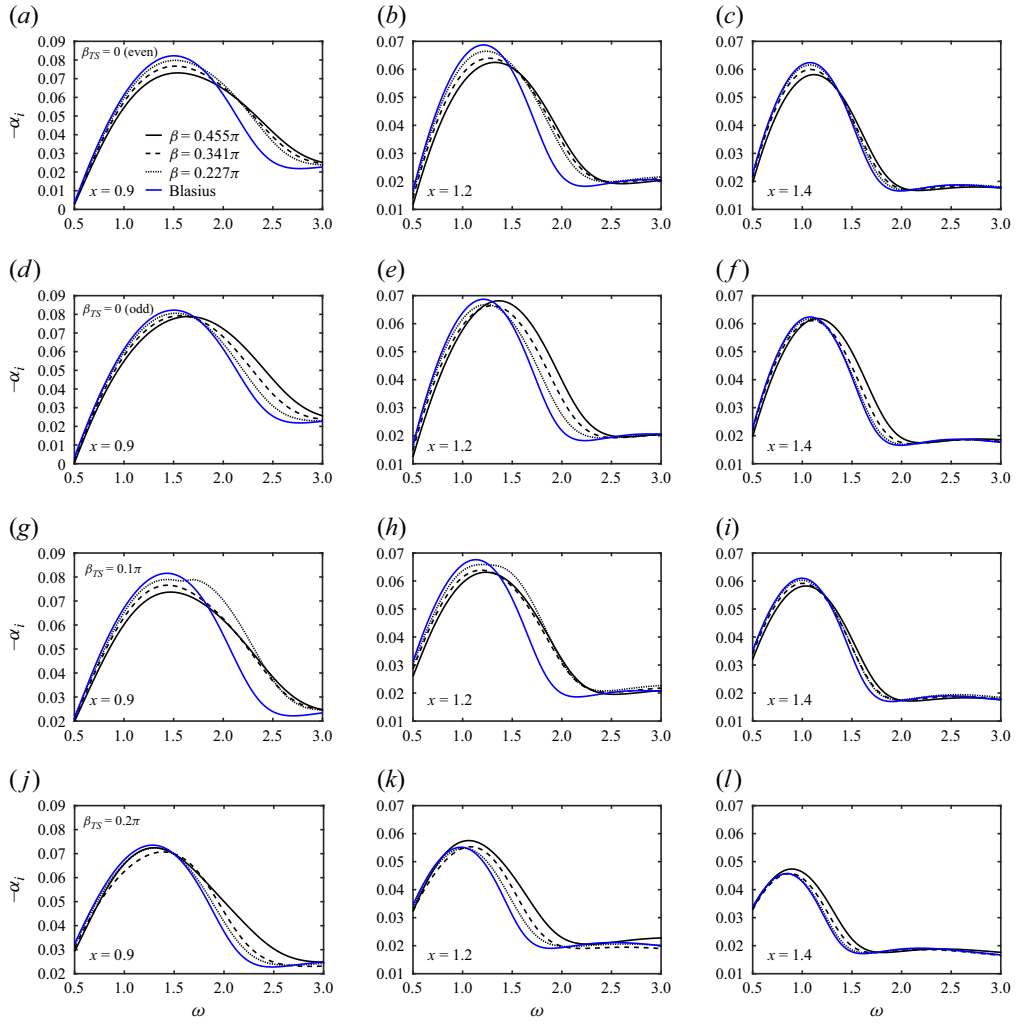


Figure 9. Local growth rates $(-\alpha_i)$ versus the frequency ω of planar ($\beta_{TS} = 0$) and oblique modes at various streamwise positions. (*a–c*) Symmetric (even) modes; (*d–f*) antisymmetric (odd) modes; (*g–i*) $\beta_{TS} = 0.1\pi$; (*j–l*) $\beta_{TS} = 0.2\pi$. Curves: blue solid, Blasius; black solid, $\beta = 0.455\pi$; black dashed, $\beta = 0.341\pi$; black dotted, $\beta = 0.227\pi$. The roughness height $h = 0.095$.

represented by the black solid and dashed lines indicates that roughness arrays of greater height have stronger effects on linear stability.

Figure 9 shows the local growth rates for roughness elements with the same height $h = 0.095$ but different spanwise wavenumbers, $\beta = 0.455\pi$, 0.341π and 0.227π. For 2-D modes, roughness elements with larger spanwise wavenumbers have a stronger stabilising/destabilising effect on the linear stability in the lower/higher frequency band. The switchover between the stabilising and destabilising effects exhibits again a weak dependence on β. This trend remains for weakly oblique modes with $\beta_{TS} = 0.1\pi$, as shown in figure 9(*g–i*). However, the arrays with $\beta = 0.227\pi$ appear somewhat out of line as the switchover occurs at a lower frequency than that for $\beta = 0.341\pi$ and 0.455π. For stronger oblique modes with $\beta_{TS} = 0.2\pi$, roughness elements slightly inhibit lower-frequency modes, but appreciably destabilise higher-frequency ones, and this effect is

https://doi.org/10.1017/jfm.2026.11174 Published online by Cambridge University Press

stronger for larger β. Overall, roughness arrays having the same height but different spanwise wavenumbers play a qualitatively similar role, but the quantitative extent of their influence depends on β_{TS} and β, the spanwise wavenumbers of the modes and the roughness arrays.

The viscous instability is controlled by the wall shear and the geometry of the roughness elements, which are determined by two parameters, height h and spanwise wavenumber β. The studies mentioned above monitored effects of h for a fixed β (figure 8) and of β for a fixed h (figure 9). A close inspection of the mathematical description suggests that the roughness-induced spanwise pressure gradient and slip velocity driving the spanwise motion in the boundary layer are proportional to h (if h is assumed small), and so the streaks, forced through the continuity equation, must be proportional to $h\beta$. It follows that the wall shear and the geometric effect (represented by hF_Z) both scale as $h\beta$. It is thus tempting to consider the product $h\beta$ as the relevant parameter for characterising the effect of roughness arrays on the instability. However, it should be noted that this proposition is underpinned by taking $h \ll 1$ and the observation that β appears on its own in the stability equations. In what follows, we address the question: to what degree is the proposition valid?

We performed calculations for roughness arrays with different height h and spanwise wavenumber β: $(h, \beta) = (0.055, 0.909\pi)$, $(0.11, 0.455\pi)$ and $(0.22, 0.227\pi)$, for all of which the product $h\beta = 0.05\pi$. The local growth rates are shown in figure 10. For planar symmetric modes with low frequencies, the growth rates for the three cases collapse perfectly into a single curve (figure 10*a–c*). However, when the frequency exceeds a critical value, the results differ, and roughness arrays with smaller β (i.e. large spanwise spacing) have stronger destabilising effects. Surprisingly, the growth rates of odd modes completely overlap for all frequencies (figure 10*d–f*), indicating that $h\beta$ is the sole relevant parameter in this case. Weakly oblique modes ($\beta_{TS} = 0.1\pi$) exhibit a similar dependence on $h\beta$ (figure 10*g–i*) to the planar even modes. For stronger oblique modes with $\beta_{TS} = 0.2\pi$ (figure 10*j–l*), the growth rate is primarily dependent on the product $h\beta$, exhibiting appreciable but insignificant difference from case to case only at the high-frequency end.

7.2. *Spatial development and the change of N-factor*

In order to characterise further the effect of roughness elements on instability, we now trace the development of upstream TS modes into the streaky region. Six modes are selected with frequencies $\omega = 0.5$, 1, 1.5, 2, 2.5 and 3. Their growth rates as a function of x are displayed in figure 11. The results show once again, but from a different perspective, that 2-D symmetric modes ($\omega = 0.5$ and 1, shown in figure 11*a*,*b*) are stabilised on entering the streaky region. The stabilising effect operates in the region before or just slightly after the mode acquires its maximum growth rate. However, for $\omega = 1.5$ (figure 11*c*), the mode is first inhibited and then enhanced by the roughness elements, which play a destabilising role overall. For larger frequencies ($\omega = 2$, 2.5 and 3, shown in figure 11*d–f*), the modes are hardly affected by the roughness arrays before reaching their respective peak growth rates, downstream of which they are destabilised. Similar trends are observed for the 2-D antisymmetric and 3-D modes, the results for which are shown in the supplementary material available at https://doi.org/10.1017/jfm.2026.11174.

To investigate the overall effects of roughness elements on the modes, we monitor the change of N-factor, defined as

$$\Delta N(\omega, \beta_{TS}) = \epsilon^{-3} \int_{x_0}^{x_1} [-\alpha_i - (-\alpha_{i,0})] \mathrm{d}x, \tag{7.2}$$

https://doi.org/10.1017/jfm.2026.11174 Published online by Cambridge University Press

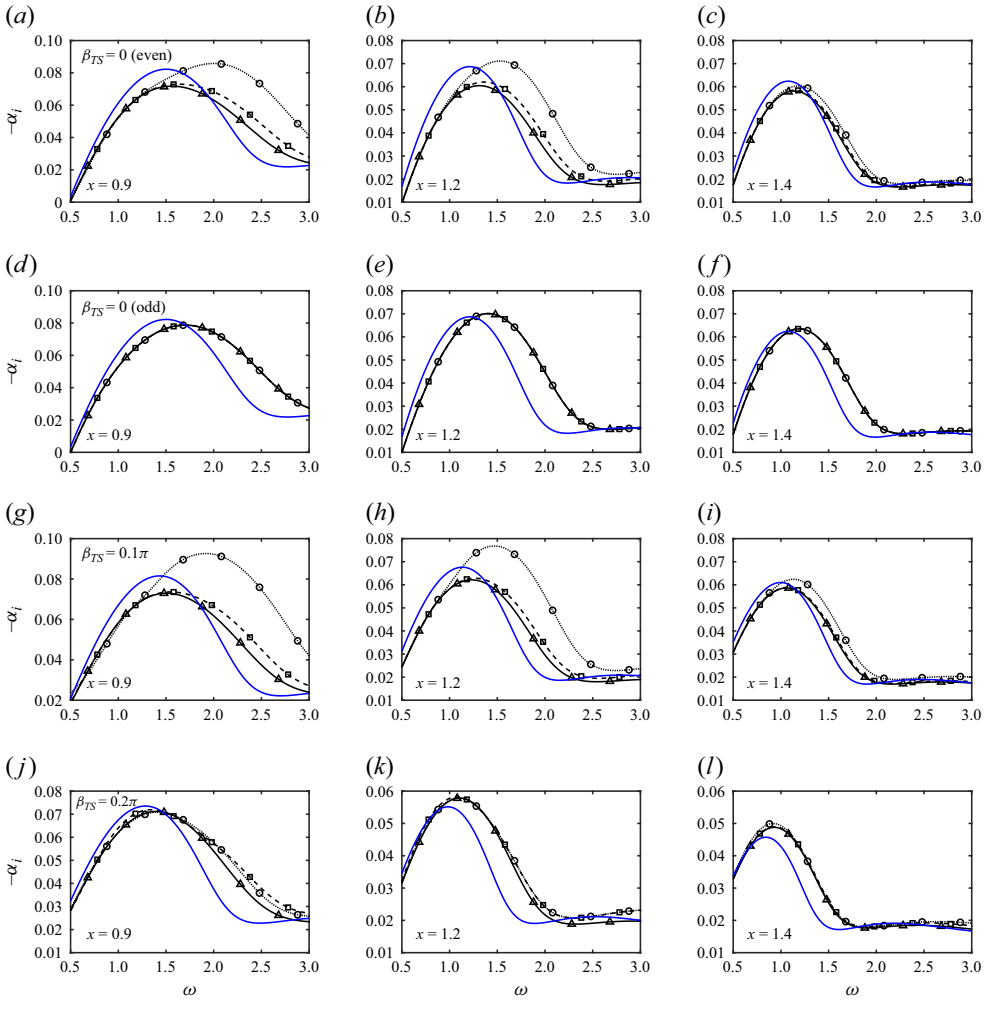


Figure 10. Local growth rates ($-\alpha_i$) versus the frequency ω of planar ($\beta_{TS}=0$) and oblique modes at various streamwise positions. (*a–c*) Symmetric (even) modes; (*d–f*) antisymmetric (odd) modes; (*g–i*) $\beta_{TS}=0.1\pi$; (*j–l*) $\beta_{TS}=0.2\pi$. Curves: blue solid, Blasius; black solid line with triangle, $(h,\,\beta)=(0.055,\,0.909\pi)$; black dashed line with square, $(h,\,\beta)=(0.11,\,0.455\pi)$; black dotted line with circle, $(h,\,\beta)=(0.22,\,0.227\pi)$.

where x_0 and x_1 represent upstream and downstream locations sufficiently far from the roughness elements, respectively. The local growth rates in the streaky and flat-plate cases are denoted by $-\alpha_i$ and $-\alpha_{i,0}$, respectively.

For the Gaussian-like and sinusoidal arrays (Roughness 1), we calculate the variation of ΔN with ω for representative modes with $\beta_{TS}=0$, 0.1π and 0.2π; here, the roughness-array parameters correspond to those in figures 8–10. The results are displayed in figure 12. The first column is pertinent to arrays with the same spanwise wavenumber but different heights. The integration range is set to be $(x_0,\,x_1)=(0.01,\,1.48)$, where $x_1=1.48$ is very close to the separation point. The second column presents the ΔN-factor for arrays having the same height but different spanwise wavenumbers, with the integration range being $(x_0,\,x_1)=(0.01,\,1.94)$. The third column displays the ΔN-factor for roughness elements with different β and h, but the same product $h\beta=0.05\pi$; the integration range is set to be $(x_0,\,x_1)=(0.01,\,1.48)$. The results shown in the three figures reaffirm that the roughness elements exert an overall stabilising effect on 2-D and 3-D low-frequency modes, while

https://doi.org/10.1017/jfm.2026.11174 Published online by Cambridge University Press

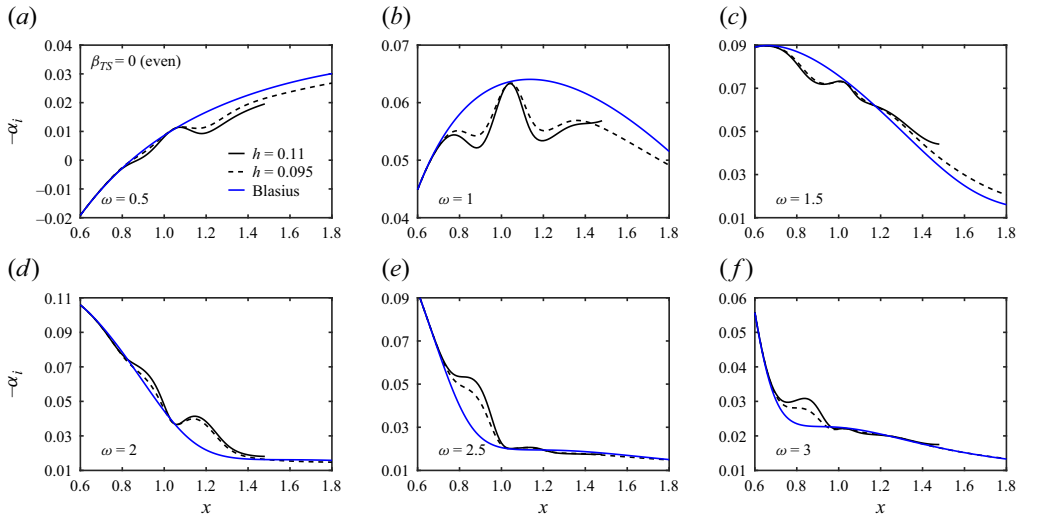


Figure 11. (*a–f*) Local growth rates ($-\alpha_i$) versus x for symmetric planar modes ($\beta_{TS}=0$). Curves: blue solid, Blasius; black solid, $h=0.11$; black dashed, $h=0.095$. The spanwise wavenumber of roughness arrays $\beta=0.455\pi$.

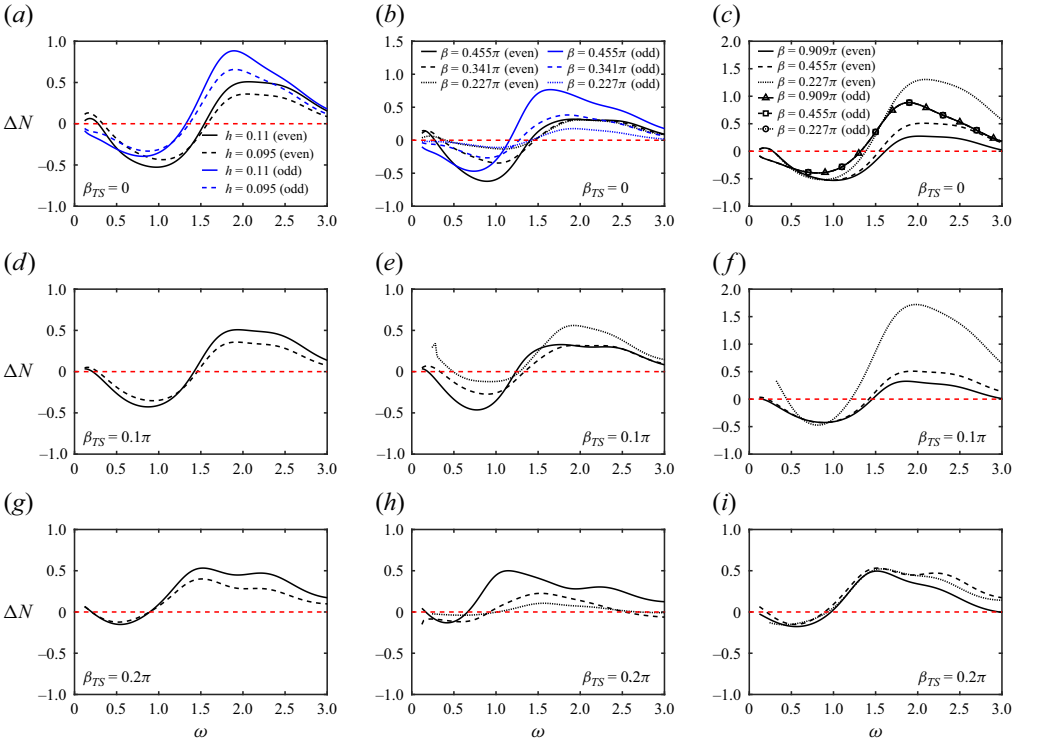


Figure 12. The ΔN-factor versus ω for representative instability modes in the case of the Gaussian-like and sinusoidal roughness. (*a–c*) $\beta_{TS}=0$; (*d–f*) $\beta_{TS}=0.1\pi$; (*g–i*) $\beta_{TS}=0.2\pi$. (*a*,*d*,*g*) $h=0.11$ and 0.095, $\beta=0.445\pi$; (*b*,*e*,*h*) $\beta=0.445\pi$, 0.341π and 0.227π, $h=0.095$; (*c*,*f*,*i*) $(h,\beta)=(0.055, 0.909\pi)$, $(0.11, 0.455\pi)$ and $(0.22, 0.227\pi)$ with $h\beta=0.157$. The parameter: $\epsilon=0.2036$.

https://doi.org/10.1017/jfm.2026.11174 Published online by Cambridge University Press

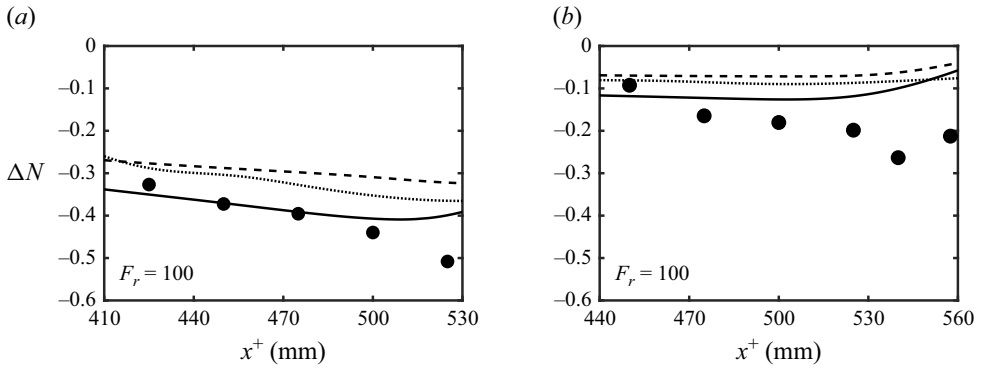


Figure 13. The ΔN-factor versus the dimensional coordinate x^+ for planar symmetric modes ($\beta_{TS} = 0$). The spanwise spacing of the arrays: (*a*) $\Lambda^+ = 15$ mm; (*b*) $\Lambda^+ = 30$ mm. Curves: black solid, step-like and hemispherical-cap roughness ($l_x = 0.28$ and $d_x = 0.1$); black dashed, step-like and sinusoidal roughness; black dotted, Gaussian-like and sinusoidal roughness ($d = 0.2$); circles, experimental results ($l_x^+ = 250$ mm and $h^+ = 1$ mm) of Downs & Fransson (2014). Parameters used in our calculations: $h = 0.12$ ($h^+ = 0.43$ mm), $\Lambda = 4.4/8.8$ and $\epsilon = 0.2036$.

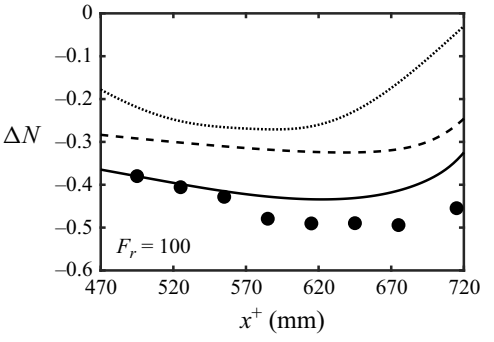


Figure 14. The ΔN-factor versus x^+ for planar symmetric modes ($\beta_{TS} = 0$). Curves: black solid, step-like and hemispherical-cap roughness ($l_x = 0.4$ and $d_x = 0.1$); black dashed, step-like and sinusoidal roughness; black dotted, Gaussian-like and sinusoidal roughness ($d = 0.3$); circles, experimental results ($l_x^+ = 480$ mm and $h^+ = 1$ mm) of Downs & Fransson (2014). Parameters used in our calculations: $h = 0.103$ ($h^+ = 0.43$ mm), $\Lambda = 3.6$ and $\epsilon = 0.1976$.

destabilising most of the other modes. Higher roughness arrays produce stronger effects. However, the effect of the spanwise wavenumber β does not follow a monotonic trend.

7.3. *Comparison with the experimental results of Downs & Fransson (2014)*

7.3.1. *Comparison of ΔN values*

Downs & Fransson (2014) showed that the leading and trailing edges of the roughness elements induce an enhanced amplification, the reason for which is not entirely clear. However, over the central part of the roughness elements, $420\,\text{mm} < x^+ < 540$ mm and $470\,\text{mm} < x^+ < 720\,\text{mm}$ for the two configurations (where $x^+ = xL$ represents the dimensional streamwise coordinate), the disturbances grow at reduced rates compared with the flat-plate case.

Figures 13–15 present a comparison of experimentally measured and theoretically predicted ΔN-factors in the central region. Computations are performed for three types of roughness configurations: Gaussian-like and sinusoidal (Roughness 1), step-like and

https://doi.org/10.1017/jfm.2026.11174 Published online by Cambridge University Press

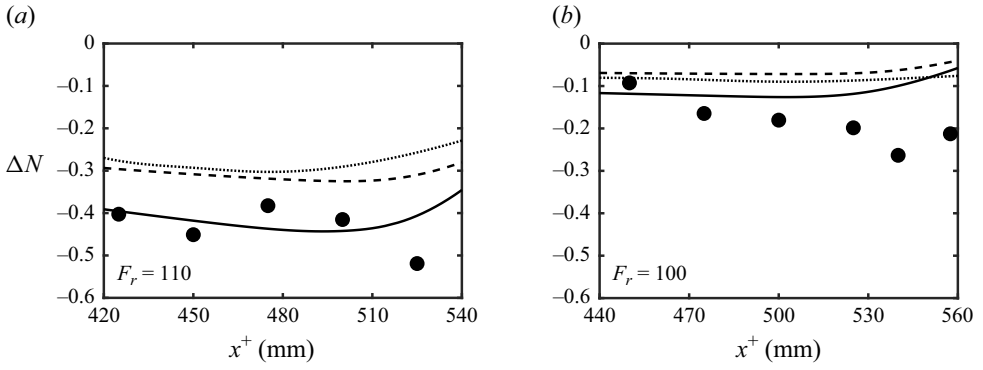


Figure 15. The ΔN-factor versus x^+ for planar symmetric modes ($\beta_{TS} = 0$) for different frequencies: (*a*) $F_r = 110$; (*b*) $F_r = 120$. Curves: black solid, step-like and hemispherical-cap roughness ($l_x = 0.28$ and $d_x = 0.1$); black dashed, step-like and sinusoidal roughness; black dotted, Gaussian-like and sinusoidal roughness ($d = 0.2$); circles, experimental results ($l_x^+ = 250$ mm and $h^+ = 1$ mm) of Downs & Fransson (2014). Parameters used in our calculations: $h = 0.12$ ($h^+ = 0.43$ mm), $\Lambda = 4.4$ and $\epsilon = 0.2036$.

hemispherical-cap (Roughness 2) and step-like and sinusoidal (Roughness 3), of which the second models the experiments closely, and is our main focus. For each configuration, the streamwise length and spanwise spacing may take two values. The experimental data are extracted from figures 10, 13 and 16 in Downs & Fransson (2014). Overall, the theoretical predictions agree with the measurements qualitatively in terms of general trends, while appreciable quantitative discrepancies are noted. Theoretical results in figure 13 indicate that the ΔN-factor decreases with the spanwise spacing of the roughness array. Furthermore, figure 14 demonstrates that for longer roughness arrays, both theoretical and experimental results feature an extended region of negative ΔN-factor, indicating a more substantial stabilising effect on TS waves. Figure 15 presents the results for higher-frequency modes, which are similar to those in figure 13(*a*).

The comparison between the three configurations underscores the influence of both the streamwise and spanwise patterns of roughness arrays on the ΔN-factor. The second configuration turns out to be consistently most effective. Comparing the step-like and sinusoidal arrays with the Gaussian-like and sinusoidal arrays (figures 13*a* and 15), we note that the difference of the ΔN-factor becomes larger with increasing frequency. This behaviour is attributed to the fact that the maximum growth rate of higher-frequency modes is located closer to the leading edge of the flat plate, where the step-like distribution has a greater influence on the base flow than the Gaussian-type distribution.

Note that the heights used in our calculations are a little less than half of the experimental ones, but the theoretically calculated ΔN values for some cases are higher than the experimental measurements in some cases. There are several possible reasons for the quantitative discrepancy. The first may be attributed to the presence of a weak but appreciable adverse pressure gradient in the experiments. The effect of the latter may be non-negligible since boundary-layer instability is known to be sensitive to it. The second reason may be the inherent non-parallelism of the streaky boundary layer, and different ways of defining the ΔN-factor in the theory and experiment. In our formulation, the non-parallelism of the streaky flow is neglected and ΔN is calculated using the local modal growth rate, which is independent of the wall-normal and spanwise positions. In the experiments, the N-factor was first computed using the local amplitude of the disturbance. The latter may be measured differently, and in Downs & Fransson (2014) it was taken to be the root mean square of the fluctuation integrated across the boundary layer and one spanwise period. The difference between the N-factors with and without roughness arrays

https://doi.org/10.1017/jfm.2026.11174 Published online by Cambridge University Press

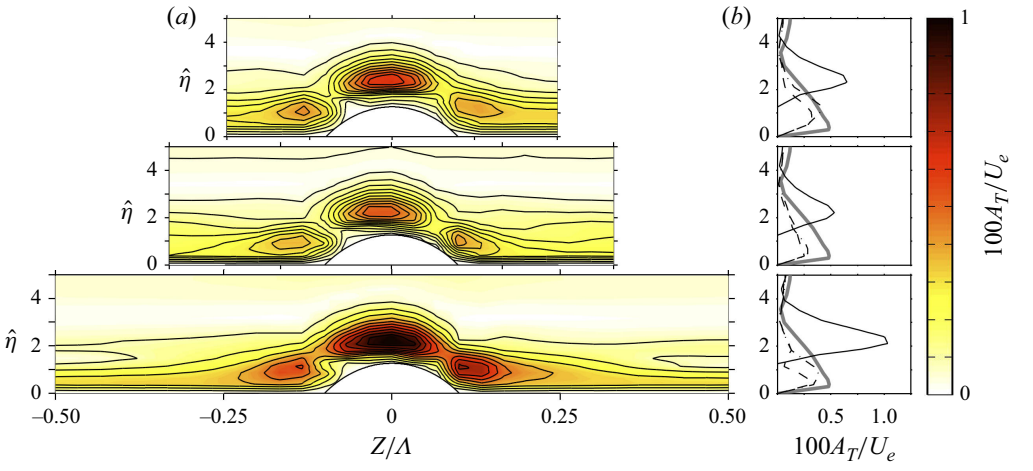


Figure 16. Experimental results of Downs & Fransson (2014): (*a*) contours of the TS-wave amplitude, A_T, at the streamwise locations $x = 1.17$ ($x^+ = 500$ mm), where U_e is the slip velocity. The reader is referred to Downs & Fransson (2014) for the definitions of these quantities. The spanwise periods of the first, second and third rows in each panel are $\Lambda^+ = 15$, 20 and 30 mm, respectively. The spacing $\Lambda = 4.2$, 5.6 and 8.4, respectively. The curves in (*b*) show the profile of the TS-wave amplitude along $Z/\Lambda = 0$ (thin solid line), $Z/\Lambda = 1/4$ (dot-dashed line) and $Z/\Lambda = 1/2$ (dashed line). The thick solid line represents the eigenfunction of the undistorted TS mode in the absence of roughness, which is included as a reference. The TS-wave frequency $\omega \approx 1.4$.

was taken to be ΔN. Clearly, the N- and ΔN-factors were affected by the non-parallelism. Furthermore, the fluctuations measured likely consist of non-modal components. We note that the asymptotic theory can be extended to account for effects of both pressure gradient and non-parallelism. Finally, the discrepancy could be due to the rather moderate Reynolds number considered, and/or the limitation of the lower-branch scaling regime adopted. Figure 16(*c*) of Downs & Fransson (2014) shows that the amplitude is already undergoing attenuation near $x^+ \approx 550$ mm, indicating the proximity to the upper branch of the neutral curve. The instability may have to be described by a five-deck asymptotic structure (Smith & Bodonyi 1982; Bodonyi, Smith & Gajjar 1983). This prospect is left for future investigation.

7.3.2. *Comparison of eigenfunctions*

Figure 16 shows the key measurements of Downs & Fransson (2014): contours of TS-wave amplitude (figure 16*a*) and TS-wave profiles (figure 16*b*) for a mode with $\omega \approx 1.4$ at $x = 1.17$ ($x^+ = 500$ mm). The spanwise spacings of the roughness arrays are $\Lambda^+ = 15$, 20 and 30 mm. The relevant characteristics are commented on when we present our theoretical results. To facilitate comparisons with the experiment, the leading-order lower- and main-deck solutions for the streamwise velocity are combined to construct a composite solution, valid in both the main and lower decks:

$$U_c = \bar{U}_d(\bar{Y}) + U_d(Y) - \lambda_u A_1, \tag{7.3}$$

where $\bar{U}_d$ and U_d are given by (6.8*a*) and (6.20), respectively, while the third term is the common part of $\bar{U}_d$ and U_d. The solution is written in terms of $\hat{\eta}$ with $\bar{Y}$ and Y being converted to $\hat{\eta}$, where $\hat{\eta} = (Y + \epsilon^{-1}hF)/\sqrt{x}$. The value of ϵ used in the conversion is taken to be 0.2036, which corresponds to $Re = 3.4 \times 10^5$.

Figures 17–19 show the distribution of the eigenfunction U_c of a symmetric mode with $\omega = 1.4$ and $\beta_{TS} = 0$ in the case of step-like and hemispherical-cap roughness ($l_x = 0.28$,

https://doi.org/10.1017/jfm.2026.11174 Published online by Cambridge University Press

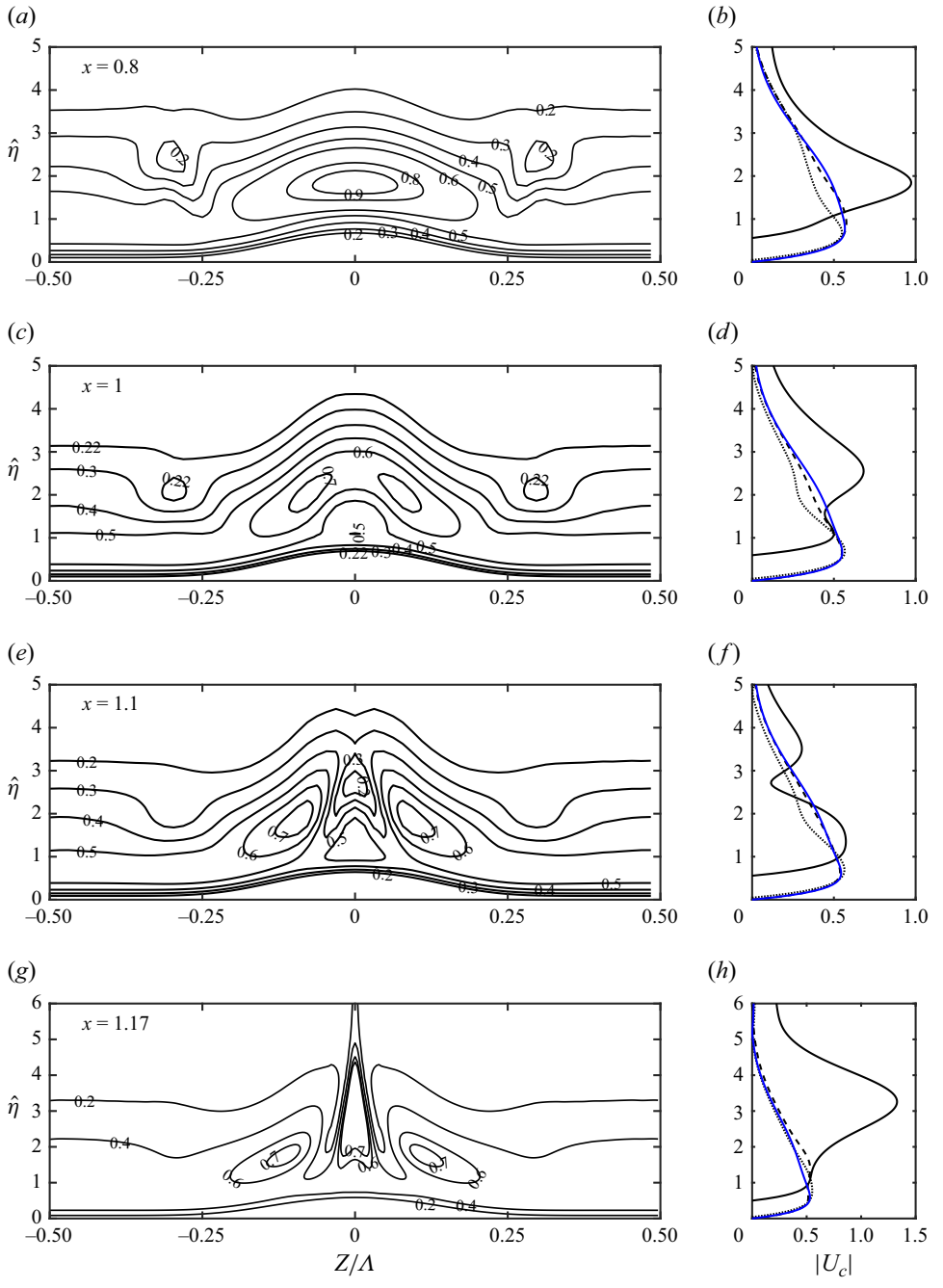


Figure 17. Eigenfunction of the symmetric mode with $\omega = 1.4$ and $\beta_{TS} = 0$ for the step-like and hemispherical-cap roughness ($l_x = 0.28$, $d_x = 0.1$). (a,c,e,g) Contours of $|U_c|$ in the $\hat{\eta}-Z$ plane; (b,d,f,h) profiles of $|U_c|$ at $Z/\Lambda = 0$ (solid line), 1/4 (dotted line) and 1/2 (dashed line). The blue solid line represents the eigenfunction of the undistorted TS mode in the absence of roughness, which is included as a reference. Parameters used in our calculations: $h = 0.12$ ($h^+ = 0.43$ mm) and $\Lambda = 4.4$.

https://doi.org/10.1017/jfm.2026.11174 Published online by Cambridge University Press

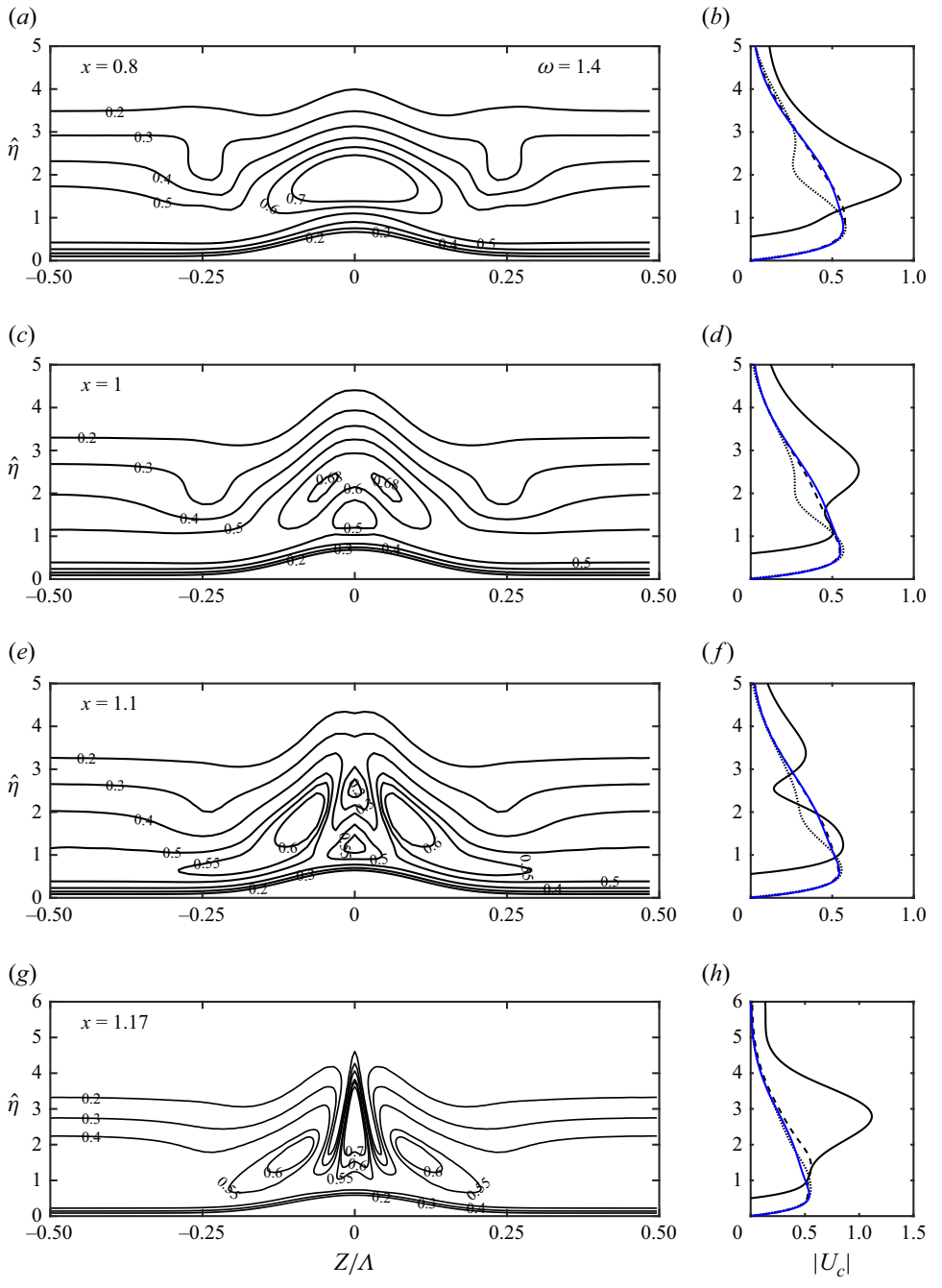


Figure 18. Eigenfunction of the symmetric mode with $\omega = 1.4$ and $\beta_{TS} = 0$ for the step-like and hemispherical-cap roughness ($l_x = 0.28$, $d_x = 0.1$). (a,c,e,g) Contours of $|U_c|$ in the $\hat{\eta}-Z$ plane; (b,d,f,h) profiles of $|U_c|$ at $Z/\Lambda = 0$ (solid line), 1/4 (dotted line) and 1/2 (dashed line). The blue solid line represents the eigenfunction of the undistorted TS mode in the absence of roughness, which is included as a reference. Parameters used in our calculations: $h = 0.12$ ($h^+ = 0.43$ mm) and $\Lambda = 6$.

https://doi.org/10.1017/jfm.2026.11174 Published online by Cambridge University Press

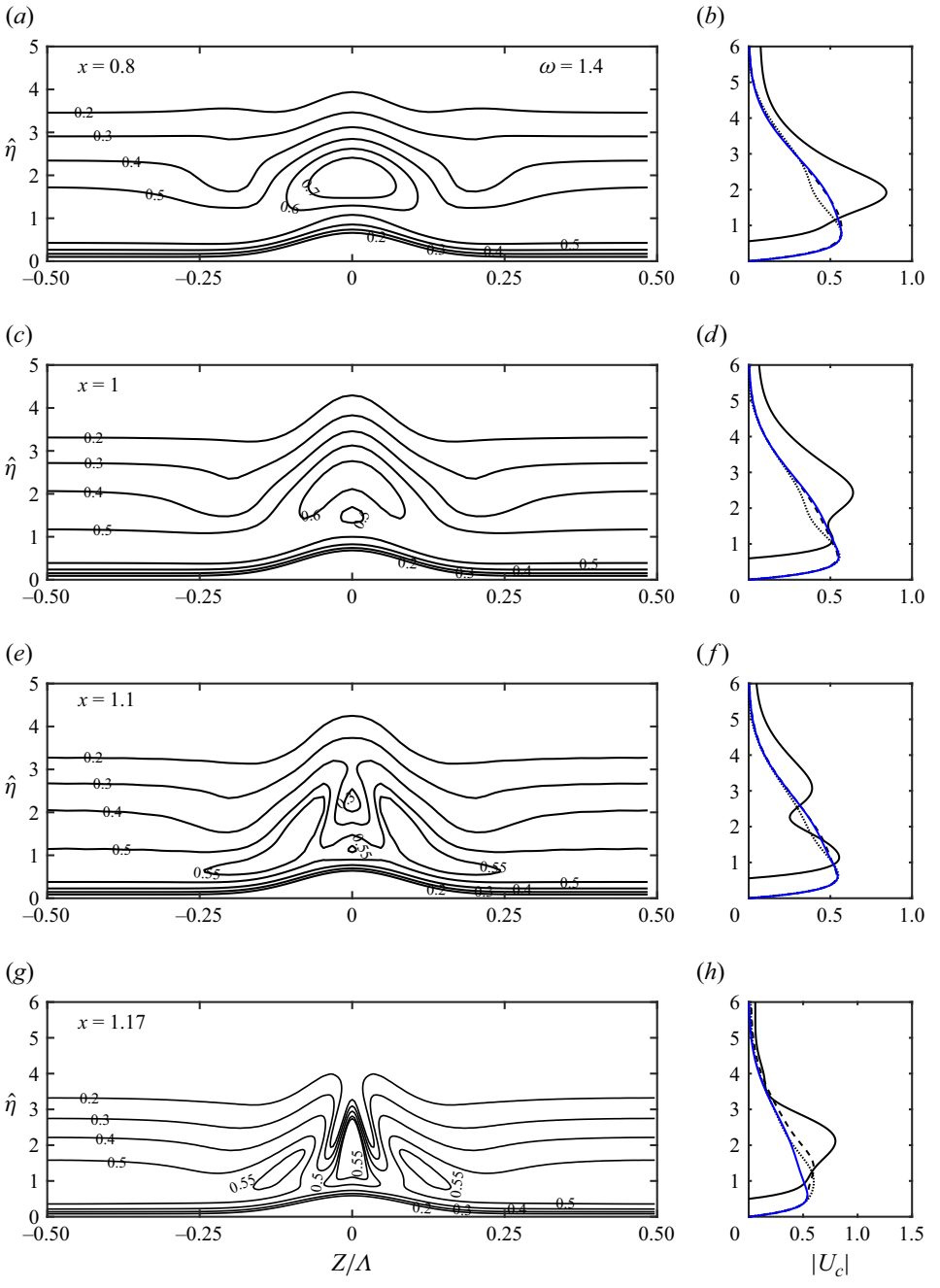


Figure 19. Eigenfunction of the symmetric mode with $\omega = 1.4$ and $\beta_{TS} = 0$ for the step-like and hemispherical-cap roughness ($l_x = 0.28$, $d_x = 0.1$). (a,c,e,g) Contours of $|U_c|$ in the $\hat{\eta}-Z$ plane; (b,d,f,h) profiles of $|U_c|$ at $Z/\Lambda = 0$ (solid line), 1/4 (dotted line) and 1/2 (dashed line). The blue solid line represents the eigenfunction of the undistorted TS mode in the absence of roughness, which is included as a reference. Parameters used in our calculations: $h = 0.12$ ($h^+ = 0.43$ mm) and $\Lambda = 8.8$.

https://doi.org/10.1017/jfm.2026.11174 Published online by Cambridge University Press

$d_x = 0.1$ and $h = 0.12$) with spanwise spacing $\Lambda = 4.4$ (figure 17), 6 (figure 18) and 8.8 (figure 19). The results include contours in the $\hat{\eta}-Z$ plane (left-hand column) and typical wall-normal profiles (right-hand column) at $x = 0.8$, 1, 1.1 and 1.17.

Upstream of the roughness peak, there is a single maximum per spanwise wavelength with the eigenfunction concentrating at $Z/\Lambda = 0$ (panel (a) of figures 17–19). The modal shape undergoes significant distortion downstream, the process of which depends on the form of the spanwise spacing and height of the roughness arrays. Distortion occurs from $x = 1$ to 1.17. The central maximum splits into two off-centre maxima, followed by the emergence of a new central maximum as shown in panels (c–g) of figures 17–19. The overall feature, the presence of three maxima, resembles the experimental measurements of Downs & Fransson (2014) (figure 16). However, differences in details can be noted. The disturbance predicted exhibits high spanwise gradients between the adjacent maxima, and becomes highly localised at $Z/\Lambda = 0$, where eigenfunction contours feature a cusp (see panel (g) of figures 17 and 18), which is due to the like focusing behaviour of the streaks as shown in figure 3. Comparison of figures 17–19 suggests that the sharpness of the cusp decreases with the spanwise spacing, and in particular a cusp does not appear for the widest spacing (figure 19g).

Now we turn to profiles of modal disturbances. The predicted profiles at various spanwise positions bear broadly similar characteristics to those observed in the experiments (cf. profiles shown in figures 17h and 18h and figure 16). The profiles differ appreciably from that of the usual undistorted TS mode. The profile at $Z/\Lambda = 0$ stands out as it has a greater magnitude, and features a prominent peak at larger distances to the wall ($\hat{\eta} \approx 3$) compared with those at other spanwise locations.

While the salient overall features of the experimental measurements of Downs & Fransson (2014) are captured qualitatively by the theory, differences in details can be noted. The disturbance predicted exhibits significant spanwise focusing, leading to high spanwise gradients between the adjacent maxima, which is not present in the experimental data. The difference may be due to the limitation of the present asymptotic approach of boundary-layer type, which does not fully account for the spanwise diffusion (ellipticity). This approximation is no longer valid when the focusing-induced spanwise gradients become strong and a new asymptotic theory that accounts for the full effect of the shorter spanwise scale must be developed. This issue is left as a topic for future investigation.

8. Conclusions

The present paper was motivated by recent experimental observations and numerical simulations, which suggest spanwise-modulated streaks may inhibit the amplification of TS modes and significantly delay transition to turbulence. We carried out a theoretical study of the delaying mechanism based on the high-Reynolds-number asymptotic approach, focusing on the lower-branch viscous instability of the streaky boundary layer induced by streamwise-grooved and spanwise-periodic roughness arrays. The spanwise spacing of the arrays was set to be comparable to the characteristic wavelength of TS modes, while the streamwise length scale corresponded to that of the undistorted boundary layer. The asymptotic threshold height ensuring that the streaky wall shear is altered by $O(1)$ is of $O(Re^{-3/8}L)$, much greater than the boundary-layer thickness.

In the presence of the specified roughness elements, the asymptotic structure of the streaky base flow consists of the viscous boundary layer and an inviscid upper deck, rather than triple decks. Perturbations in the inviscid upper deck are nonlinear, but irrotational so that they are governed by a 2-D Laplace equation in the transverse

https://doi.org/10.1017/jfm.2026.11174 Published online by Cambridge University Press

plane for the streamfunction, whose solution is directly determined by the roughness elements. The streaky base flow in the viscous boundary layer is governed by the 3-D nonlinear boundary-layer equations, which are solved numerically using an efficient streamwise marching method. Numerical results showed that the streaky flow consists of spanwise alternating low- and high-speed regions, and the streaks undergo spanwise focusing, as a result of which boundary-layer separation of the 'collision type' may occur sufficiently downstream.

Linear stability analysis was performed to investigate the evolution of the lower-branch viscous TS modes through the streaky base flow. By exploiting the asymptotic structure, we analytically resolved the dependence of the instability mode on the wall-normal variable so that the bi-global eigenvalue problem is reduced to a one-dimensional one. The instability is found to be controlled by the spanwise-dependent wall shear and the shape function of the roughness arrays. Numerical results showed that 2-D and weakly 3-D low-frequency TS modes are stabilised by roughness elements, while most of the other modes are destabilised. Roughness arrays with greater heights lead to stronger stabilising and destabilising effects. Arrays with shorter spanwise spacing exert a stronger stabilising effect on weakly 3-D low-frequency modes and a weaker destabilising effect on weakly 3-D higher-frequency modes, but a stronger destabilising effect on strongly 3-D modes.

The asymptotically reduced mathematical systems avoid meshing a curved boundary and allow us to predict efficiently the streaky base flow and furthermore to assess quickly their impact on the lower-branch viscous instability. The approach complements DNS and laboratory studies in that it establishes the ultimate instability property at arbitrarily large Reynolds numbers and provides *a priori* insight into the dominant transition delaying mechanism.

Based upon formal asymptotic approximation, the present theory is self-justified in that its validity is guaranteed for sufficiently large Reynolds numbers, but its accuracy at moderate Reynolds numbers needs to be further quantified through comparison with DNS and experimental data. Preliminary comparisons with experimental data performed in the paper indicated that the theory captured the trends and provided qualitatively accurate predictions. Possible reasons for quantitative discrepancies were discussed, and these included, apart from uncertainties in laboratory measurements, moderate Reynolds numbers, effects of pressure gradient and non-parallelism as well as the limitations of the boundary-layer type of approximation and lower-branch scaling regime. Further theoretical refinement is required to account for the pressure gradient, non-parallel flow and spanwise ellipticity effects as well as to cover the upper-branch scaling regime. It is hoped that the present work will promote further laboratory and computational investigations so that appropriate and thorough comparisons will become possible in the near future.

The present work, along with those of Kátai & Wu (2020) and Zheng & Wu (2024), has investigated the lower-branch viscous instability of streaky boundary layers over spanwise-periodic and streamwise-elongated roughness arrays with the spanwise spacing Λ^+ being of $O(Re^{-3/8}L)$. This instability operates in the region where $L = O((U_\infty \Lambda^+/\nu)^{3/5}\Lambda^+)$ for a fixed dimensional Λ^+. As instability modes evolve downstream, they may enter a distinguished upper-branch regime due to the gradual increase of the boundary-layer thickness; this regime commences where $\Lambda^+ = O(Re^{-9/20}L)$, i.e. $L = O((U_\infty \Lambda^+/\nu)^{9/11}\Lambda^+)$ for a fixed Λ^+. Moreover, roughness arrays may either impact existing, or even induce new, inviscid instability in the region farther downstream where $L = O((U_\infty \Lambda^+/\nu)\Lambda^+)$, i.e. $\Lambda^+ = O(Re^{-1/2}L)$. Both topics are being investigated in our ongoing work.

https://doi.org/10.1017/jfm.2026.11174 Published online by Cambridge University Press

Supplementary material. Supplementary material is available at https://doi.org/10.1017/jfm.2026.11174.

Acknowledgements. The authors would like to thank the referees for their comments and suggestions, which have helped us improve the paper.

Funding. This investigation was supported by NSFC (grant nos. 12272187 and 91952202).

Declaration of interests. The authors report no conflict of interest.

Appendix A. Upstream conditions

As the roughness height diminishes in the upstream limit, deviation from (f_B, U_B) is small such that $(f_1, g_1, U_1, W_1) \ll 1$. Therefore, (3.14) simplify to the linearised form

$$xU_B\frac{\partial U_1}{\partial x}-\frac{1}{2}f_B\frac{\partial U_1}{\partial \eta}-\frac{\partial^2 U_1}{\partial \eta^2}=\left(\frac{1}{2}f_1+x\frac{\partial f_1}{\partial x}+x\frac{\partial g_1}{\partial Z}\right)\frac{\partial U_B}{\partial \eta}, \tag{A1a}$$

$$xU_B\frac{\partial W_1}{\partial x}-\frac{1}{2}f_B\frac{\partial W_1}{\partial \eta}-\frac{\partial^2 W_1}{\partial \eta^2}=-xP_Z. \tag{A1b}$$

On the other hand, solving the linearised version of (2.11) over a practically flat surface $y=0$, the spanwise pressure gradient at $y=0$ is found as (Kátai & Wu 2020)

$$P_Z=\frac{h}{\pi}\fint_{-\infty}^{\infty}\frac{F_{xx}(x,\xi)}{\xi-Z}\mathrm{d}\xi. \tag{A2}$$

A similarity solution to (A1)–(A2) is now constructed. In view of (3.17), the solution assumes the like form

$$(g_1, W_1)=hS'(Z)T(x)\big(M(\eta), M'(\eta)\big),\quad (f_1, U_1)=hS''(Z)Q(x)\big(G(\eta), G'(\eta)\big), \tag{A3a,b}$$

where $S'(Z)$ is given by

$$S'(Z)=\frac{1}{\pi}\fint_{-\infty}^{\infty}\frac{F_g(\xi)}{\xi-Z}\mathrm{d}\xi, \tag{A4}$$

which is computed using

$$F_g=\sum_{n=-\infty}^{\infty}F_{g,n}\exp(\mathrm{i}n\beta Z),\quad S'(Z)=\sum_{n=-\infty}^{\infty}\mathrm{sgn}(n)F_{g,n}\exp(\mathrm{i}n\beta Z). \tag{A5}$$

As an illustration, we consider a surface shape defined by (4.1), for which

$$F_f(x)=x^2\exp(-(x-1+d^2)^2/d^2+d^2)\sim a_0x^2\quad\text{as}\quad x\to 0, \tag{A6}$$

where d is a parameter characterising the sharpness of the peak attained at $x=1$ and $a_0=\exp(2-d^{-2})$. Inserting (A3) and (A6) into (A1) shows that a similarity solution exists with $T(x)=2a_0x$ and $Q(x)=2a_0x^2$, and that G and M satisfy the ordinary differential equations

$$2U_B\frac{\partial G}{\partial \eta}-\frac{1}{2}f_B\frac{\partial^2 G}{\partial \eta^2}-\frac{\partial^3 G}{\partial \eta^3}=\left(\frac{5}{2}G+M\right)\frac{\partial U_B}{\partial \eta}, \tag{A7a}$$

$$U_B\frac{\partial M}{\partial \eta}-\frac{1}{2}f_B\frac{\partial^2 M}{\partial \eta^2}-\frac{\partial^3 M}{\partial \eta^3}=-1. \tag{A7b}$$

https://doi.org/10.1017/jfm.2026.11174 Published online by Cambridge University Press

It follows from (3.16) and (A3) that the boundary conditions for (A7) are

$$G(0)=0,\quad G'(0)=0,\quad G'(\infty)=0;\quad M(0)=0,\quad M'(0)=0,\quad M'(\infty)=-1, \tag{A8}$$

where $M'(\infty)=-1$ follows from the balance $\partial W_1/\partial x=-\partial P/\partial Z$ in (A1*b*) as $\eta\to\infty$. The boundary-value problem (A7)–(A8) is solved numerically using the fourth-order Runge–Kutta scheme and a shooting method.

In summary, the velocities in the upstream region are found as

$$U_1=2a_0hx^2S''(Z)G'(\eta),\quad W_1=2a_0hxS'(Z)M'(\eta), \tag{A9}$$

which serve as the upstream condition.

For Roughness 2 and Roughness 3, in the upstream limit, the second derivative of $F_f(x)$ is given by

$$F_{f,xx}\sim-\left[\tanh z\left(\frac{l_x+1}{d_x}\right)\operatorname{sech}^2\left(\frac{l_x+1}{d_x}\right)+\tanh\left(\frac{l_x-1}{d_x}\right)\operatorname{sech}^2\left(\frac{l_x-1}{d_x}\right)\right]/d_x^2\quad\text{as}\quad x\to0, \tag{A10}$$

which is used in the upstream solution (A9) with $a_0=F_{f,xx}/2$.

Appendix B. Coefficients of (6.20)

The expressions for D_j $(j=0,1,2,3,4)$ appearing in (6.20) are found as

$$D_0=\frac{\mathrm{i}\alpha\bar{P}_d}{\left(1+h^2F_Z^2\right)^{1/3}(\mathrm{i}\alpha\lambda_u)^{2/3}\mathrm{Ai}'(\zeta_0)}-\frac{1}{\mathrm{Ai}'(\zeta_0)}\left[\zeta_0\mathrm{Ai}(\zeta_0)D_1+\zeta_0\mathrm{Gi}(\zeta_0)D_2+\frac{\zeta_0^2\mathrm{Ai}'(\zeta_0)}{4}D_3+\frac{\zeta_0^2\mathrm{Gi}'(\zeta_0)}{4}D_4+\frac{D_4-4D_2}{4\pi}\right], \tag{B1a}$$

$$D_1=\frac{\pi}{\mathrm{i}\alpha}\left(1+h^2F_Z^2\right)^{-1/3}(\mathrm{i}\alpha\lambda_u)^{-2/3}\frac{\mathrm{Gi}(\zeta_0)}{\mathrm{Ai}(\zeta_0)}\left\{\left[\frac{5}{3}\frac{\lambda_{uZ}}{\lambda_u}+\frac{2h^2F_ZF_{ZZ}}{3\left(1+h^2F_Z^2\right)}+\zeta_0\left(\frac{\mathrm{Gi}'(\zeta_0)}{\mathrm{Gi}(\zeta_0)}-\frac{\mathrm{Ai}'(\zeta_0)}{\mathrm{Ai}(\zeta_0)}\right)\left(\frac{2\lambda_{uZ}}{3\lambda_u}+\frac{2h^2F_ZF_{ZZ}}{3\left(1+h^2F_Z^2\right)}\right)\right]\frac{\partial\bar{P}_d}{\partial Z}-\frac{\partial^2\bar{P}_d}{\partial Z^2}\right\}, \tag{B2b}$$

$$D_2=\frac{\pi}{\mathrm{i}\alpha}\left(1+h^2F_Z^2\right)^{-1/3}(\mathrm{i}\alpha\lambda_u)^{-2/3}\left[\frac{\partial^2\bar{P}_d}{\partial Z^2}-\frac{\partial\bar{P}_d}{\partial Z}\left(\frac{5}{3}\frac{\lambda_{uZ}}{\lambda_u}+\frac{2h^2F_ZF_{ZZ}}{3\left(1+h^2F_Z^2\right)}\right)\right], \tag{B3c}$$

$$D_3=\frac{\pi}{\mathrm{i}\alpha}\left(1+h^2F_Z^2\right)^{-1/3}(\mathrm{i}\alpha\lambda_u)^{-2/3}\frac{\partial\bar{P}_d}{\partial Z}\frac{\mathrm{Gi}(\zeta_0)}{\mathrm{Ai}(\zeta_0)}\left(\frac{2}{3}\frac{\lambda_{uZ}}{\lambda_u}+\frac{2h^2F_ZF_{ZZ}}{3\left(1+h^2F_Z^2\right)}\right), \tag{B4d}$$

$$D_4=-\frac{\pi}{\mathrm{i}\alpha}\left(1+h^2F_Z^2\right)^{-1/3}(\mathrm{i}\alpha\lambda_u)^{-2/3}\frac{\partial\bar{P}_d}{\partial Z}\left(\frac{2}{3}\frac{\lambda_{uZ}}{\lambda_u}+\frac{2h^2F_ZF_{ZZ}}{3\left(1+h^2F_Z^2\right)}\right). \tag{B5e}$$

References

Bi, Z., Wang, P., Xu, J. & Liu, J. 2023 Three-dimensional wall heating elements effect on the instability in zero pressure gradient supersonic boundary layers. *Phys. Fluids* **35** (3), 034117.

Bodonyi, R.J., Smith, F.T. & Gajjar, J. 1983 Amplitude-dependent stability of boundary-layer flow with a strongly non-linear critical layer. *IMA J. Appl. Maths* **30** (1), 1–19.

Cossu, C. & Brandt, L. 2002 Stabilization of Tollmien–Schlichting waves by finite amplitude optimal streaks in the Blasius boundary layer. *Phys. Fluids* **14** (8), L57–L60.

https://doi.org/10.1017/jfm.2026.11174 Published online by Cambridge University Press

COSSU, C. & BRANDT, L. 2004 On Tollmien–Schlichting-like waves in streaky boundary layers. *Eur. J. Mech. B/Fluids* **23** (6), 815–833.

DOWNS, R.S. & FRANSSON, J.H.M. 2014 Tollmien–Schlichting wave growth over spanwise-periodic surface patterns. *J. Fluid Mech.* **754**, 39–74.

FRANSSON, J.H.M. 2015 Transition to turbulence delay using a passive flow control strategy. *Proc. Iutam* **14**, 385–393.

FRANSSON, J.H.M., BRANDT, L., TALAMELLI, A. & COSSU, C. 2004 Experimental and theoretical investigation of the nonmodal growth of steady streaks in a flat plate boundary layer. *Phys. Fluids* **16** (10), 3627–3638.

FRANSSON, J.H.M., BRANDT, L., TALAMELLI, A. & COSSU, C. 2005 Experimental study of the stabilization of Tollmien–Schlichting waves by finite amplitude streaks. *Phys. Fluids* **17** (5), 054110.

FRANSSON, J.H.M. & TALAMELLI, A. 2012 On the generation of steady streamwise streaks in flat-plate boundary layers. *J. Fluid Mech.* **698**, 211–234.

FRANSSON, J.H.M., TALAMELLI, A., BRANDT, L. & COSSU, C. 2006 Delaying transition to turbulence by a passive mechanism. *Phys. Rev. Lett.* **96** (6), 064501.

GOLDSTEIN, M.E. & LEIB, S.J. 1993 Three-dimensional boundary-layer instability and separation induced by small-amplitude streamwise vorticity in the upstream flow. *J. Fluid Mech.* **246**, 21–41.

GOLDSTEIN, M.E., SESCU, A., DUCK, P.W. & CHOUDHARI, M. 2016 Nonlinear wakes behind a row of elongated roughness elements. *J. Fluid Mech.* **796**, 516–557.

HANEVY, N., FERGUSON, J., TREVELYAN, P.M.J. & GRIFFITHS, P.T. 2024 Boundary-layer flows over deforming surfaces. *Phys. Rev. Fluids* **9** (5), 054101.

KÁTAI, C.B. & WU, X. 2020 Effects of streamwise-elongated and spanwise-periodic surface roughness elements on boundary-layer instability. *J. Fluid Mech.* **899**, A34.

LIN, C.C. 1946 On the stability of two-dimensional parallel flows. Part 3. Stability in a viscous fluid. *Q. Appl. Maths* **3** (4), 277–301.

LIU, J., MARENSI, E. & WU, X. 2022 Effects of streaky structures on the instability of supersonic boundary layers. In *IUTAM Laminar-Turbulent Transition* (ed. S. Sherwin, P. Schmid & X. Wu), pp. 587–598.

MULLER, D.E. 1956 A method for solving algebraic equations using an automatic computer. *Math. Tables Aids Comput.* **10** (56), 208–215.

ORSZAG, S.A. 1971 On the elimination of aliasing in finite-difference schemes by filtering high-wavenumber components. *J. Atmos. Sci.* **28** (6), 1074–1074.

PIOT, E., CASALIS, G. & RIST, U. 2008 Stability of the laminar boundary layer flow encountering a row of roughness elements: biglobal stability approach and DNS. *Eur. J. Mech. B/Fluids* **27** (6), 684–706.

PRANDTL, L. 1938 Zur Berechnung der Grenzschichten. *Angew. Math. Mech.* **18** (1), 77–82.

SATTARZADEH, S.S. & FRANSSON, J.H.M. 2017 Spanwise boundary layer modulations using finite discrete suction for transition delay. *Exp. Fluids* **58** (3), 14.

SHAHINFAR, S., FRANSSON, J.H.M., SATTARZADEH, S. & TALAMELLI, A. 2013 Scaling of streamwise boundary layer streaks and their ability to reduce skin-friction drag. *J. Fluid Mech.* **733**, 1–32.

SHAHINFAR, S., SATTARZADEH, S.S. & FRANSSON, J.H.M. 2014 Passive boundary layer control of oblique disturbances by finite-amplitude streaks. *J. Fluid Mech.* **749**, 1–36.

SHAHINFAR, S., SATTARZADEH, S.S., FRANSSON, J.H.M. & TALAMELLI, A. 2012 Revival of classical vortex generators now for transition delay. *Phys. Rev. Lett.* **109** (7), 074501.

SICONOLFI, L., CAMARRI, S. & FRANSSON, J.H.M. 2015 Stability analysis of boundary layers controlled by miniature vortex generators. *J. Fluid Mech.* **784**, 596–618.

SMITH, F.T. 1979*a* On the non-parallel flow stability of the Blasius boundary layer. *Proc. R. Soc. Lond. A* **366** (1724), 91–109.

SMITH, F.T. 1979*b* Instability of flow through pipes of general cross-section, part 1. *Mathematika* **26** (2), 187–210.

SMITH, F.T. & BODONYI, R.J. 1982 Nonlinear critical layers and their development in streaming-flow stability. *J. Fluid Mech.* **118**, 165–185.

SMITH, F.T., SYKES, R.I. & BRIGHTON, P.W.M. 1977 A two-dimensional boundary layer encountering a three-dimensional hump. *J. Fluid Mech.* **83** (1), 163–176.

SMITH, F.T. & WALTON, A.G. 1998 Flow past a two-or three-dimensional steep-edged roughness. *Proc. R. Soc. Lond. A* **454**, 31–69.

STEWARTSON, K. & SIMPSON, C.J. 1982 On a singularity initiating a boundary-layer collision. *Q. J. Mech. Appl. Maths* **35** (1), 1–16.

SZABÓ, A., NAGY, P.T., DE BAETS, M., VANIERSCHOT, G. & PAÁL, G. 2024 Stability analysis of a streaky boundary layer generated by miniature vortex generators. *Comput. Fluids* **269**, 106123.

https://doi.org/10.1017/jfm.2026.11174 Published online by Cambridge University Press

WALTON, A.G. 1996 Strongly nonlinear vortex-Tollmien–Schlichting-wave interactions in the developing flow through a circular pipe. *J. Fluid Mech.* **319**, 77–107.

WALTON, A.G. & PATEL, R.A. 1998 On the neutral stability of spanwise-periodic boundary-layer and triple-deck flows. *Q. J. Mech. Appl. Math.* **51** (2), 311–328.

WHITE, E.B. 2002 Transient growth of stationary disturbances in a flat plate boundary layer. *Phys. Fluids* **14** (12), 4429–4439.

XU, D., ZHANG, Y. & WU, X. 2017 Nonlinear evolution and secondary instability of steady and unsteady Görtler vortices induced by free-stream vortical disturbances. *J. Fluid Mech.* **829**, 681–730.

ZHENG, J. & WU, X. 2024 Effects of streamwise-elongated and spanwise-periodic surface roughness arrays on supersonic boundary-layer instability. *Phys. Fluids* **36** (5), 054115.

ZHU, K. & WU, X. 2022 Effects of spanwise-periodic surface heating on supersonic boundary-layer instability. *J. Fluid Mech.* **940**, A20.

https://doi.org/10.1017/jfm.2026.11174 Published online by Cambridge University Press